

Optimization of filtering schemes for broadband astro-combs

Guoqing Chang,^{1,2,*} Chih-Hao Li,³ David F. Phillips,³ Andrew Szentgyorgyi,³ Ronald L. Walsworth,^{3,4} and Franz X. Kärtner^{1,2}

¹Department of Electrical Engineering and Computer Science and Research Laboratory of Electronics, Massachusetts Institute of Technology, 77 Massachusetts Ave, Cambridge Massachusetts 02139, USA

²DESY-Center for Free-Electron Laser Science and Department of Physics, Hamburg University, Hamburg, Germany

³Harvard-Smithsonian Center for Astrophysics, Harvard University, 60 Garden St. Cambridge Massachusetts 02138, USA

⁴Department of Physics, Harvard University, Cambridge Massachusetts 02138, USA

*guoqing@mit.edu

Abstract: To realize a broadband, large-line-spacing astro-comb, suitable for wavelength calibration of astrophysical spectrographs, from a narrowband, femtosecond laser frequency comb (“source-comb”), one must integrate the source-comb with three additional components: (1) one or more filter cavities to multiply the source-comb’s repetition rate and thus line spacing; (2) power amplifiers to boost the power of pulses from the filtered comb; and (3) highly nonlinear optical fiber to spectrally broaden the filtered and amplified narrowband frequency comb. In this paper we analyze the interplay of Fabry-Perot (FP) filter cavities with power amplifiers and nonlinear broadening fiber in the design of astro-combs optimized for radial-velocity (RV) calibration accuracy. We present analytic and numeric models and use them to evaluate a variety of FP filtering schemes (labeled as *identical*, *co-prime*, *fraction-prime*, and *conjugate* cavities), coupled to chirped-pulse amplification (CPA). We find that even a small nonlinear phase can reduce suppression of filtered comb lines, and increase RV error for spectrograph calibration. In general, filtering with two cavities *prior to* the CPA fiber amplifier outperforms an amplifier placed between the two cavities. In particular, filtering with *conjugate* cavities is able to provide <1 cm/s RV calibration error with >300 nm wavelength coverage. Such superior performance will facilitate the search for and characterization of Earth-like exoplanets, which requires <10 cm/s RV calibration error.

©2012 Optical Society of America

OCIS codes: (060.7140) Ultrafast processes in fibers; (120.6200) Spectrometers and spectroscopic instrumentation; (190.7110) Ultrafast nonlinear optics; (060.4370) Nonlinear optics, fibers.

References and links

1. M. T. Murphy, T. Udem, R. Holzwarth, A. Sismann, L. Pasquini, C. Araujo-Hauck, H. Dekker, S. D’Odorico, M. Fischer, T. W. Hänsch, and A. Manescau, “High-precision wavelength calibration of astronomical spectrographs with laser frequency combs,” *Mon. Not. R. Astron. Soc.* **380**(2), 839–847 (2007).
2. C.-H. Li, A. J. Benedick, P. Fendel, A. G. Glenday, F. X. Kärtner, D. F. Phillips, D. Sasselov, A. Szentgyorgyi, and R. L. Walsworth, “A laser frequency comb that enables radial velocity measurements with a precision of 1 cm/s,” *Nature* **452**(7187), 610–612 (2008).
3. T. Steinmetz, T. Wilken, C. Araujo-Hauck, R. Holzwarth, T. W. Hänsch, L. Pasquini, A. Manescau, S. D’Odorico, M. T. Murphy, T. Kentischer, W. Schmidt, and T. Udem, “Laser frequency combs for astronomical observations,” *Science* **321**(5894), 1335–1337 (2008).
4. D. A. Braje, M. S. Kirchner, S. Osterman, T. Fortier, and S. A. Diddams, “Astronomical spectrograph calibration with broad-spectrum frequency combs,” *Eur. Phys. J. D* **48**(1), 57–66 (2008).

5. G. Q. Chang, C.-H. Li, D. F. Phillips, R. L. Walsworth, and F. X. Kärtner, "Toward a broadband astro-comb: effects of nonlinear spectral broadening in optical fibers," *Opt. Express* **18**(12), 12736–12747 (2010).
6. T. Wilken, C. Lovis, A. Manescau, T. Steinmetz, L. Pasquini, G. Lo Curto, T. W. Hänsch, R. Holzwarth, and T. Udem, "High-precision calibration of spectrographs," *Mon. Not. R. Astron. Soc. Lett.* **405**(1), L16–L20 (2010).
7. C.-H. Li, A. G. Glenday, A. J. Benedick, G. Q. Chang, L.-J. Chen, C. Cramer, P. Fendel, G. Furesz, F. X. Kärtner, S. Korzennik, D. F. Phillips, D. Sasselov, A. Szentgyorgyi, and R. L. Walsworth, "*In-situ* determination of astro-comb calibrator lines to better than 10 cm^{-1} ," *Opt. Express* **18**(12), 13239–13249 (2010).
8. F. Quinlan, G. Ycas, S. Osterman, and S. A. Diddams, "A 12.5 GHz-spaced optical frequency comb spanning $>400 \text{ nm}$ for near-infrared astronomical spectrograph calibration," *Rev. Sci. Instrum.* **81**(6), 063105 (2010).
9. A. J. Benedick, G. Q. Chang, J. R. Birge, L.-J. Chen, A. G. Glenday, C.-H. Li, D. F. Phillips, A. Szentgyorgyi, S. Korzennik, G. Furesz, R. L. Walsworth, and F. X. Kärtner, "Visible wavelength astro-comb," *Opt. Express* **18**(18), 19175–19184 (2010).
10. G. Schettino, E. Oliva, M. Inguscio, C. Baffa, E. Giani, A. Tozzi, and P. C. Pastor, "Optical frequency comb as a general-purpose and wide-band calibration source for astronomical high resolution infrared spectrographs," *Exp. Astron.* **31**(1), 69–81 (2011).
11. S. P. Stark, T. Steinmetz, R. A. Probst, H. Hundertmark, T. Wilken, T. W. Hänsch, T. Udem, P. St. J. Russell, and R. Holzwarth, "14 GHz visible supercontinuum generation: calibration sources for astronomical spectrographs," *Opt. Express* **19**(17), 15690–15695 (2011).
12. T. Wilken, G. L. Curto, R. A. Probst, T. Steinmetz, A. Manescau, L. Pasquini, J. I. González Hernández, R. Rebolo, T. W. Hänsch, T. Udem, and R. Holzwarth, "A spectrograph for exoplanet observations calibrated at the centimeter-per-second level," *Nature* **485**(7400), 611–614 (2012).
13. G. G. Ycas, F. Quinlan, S. A. Diddams, S. Osterman, S. Mahadevan, S. Redman, R. Terrien, L. Ramsey, C. F. Bender, B. Botzler, and S. Sigurdsson, "Demonstration of on-sky calibration of astronomical spectra using a 25 GHz near-IR laser frequency comb," *Opt. Express* **20**(6), 6631–6643 (2012).
14. L.-J. Chen, G. Q. Chang, C. H. Li, A. J. Benedick, D. F. Phillips, R. L. Walsworth, and F. X. Kärtner, "Broadband dispersion-free optical cavities based on zero group delay dispersion mirror sets," *Opt. Express* **18**(22), 23204–23211 (2010).
15. G. P. Agrawal, *Nonlinear Fiber Optics* (Academic Press, San Diego, 2001), 3rd ed.
16. D. N. Schimpf, E. Seise, J. Limpert, and A. Tünnermann, "Self-phase modulation compensated by positive dispersion in chirped-pulse systems," *Opt. Express* **17**(7), 4997–5007 (2009).
17. H. Hundertmark, S. Rämmler, T. Wilken, R. Holzwarth, T. W. Hänsch, and P. St. J. Russell, "Octave-spanning supercontinuum generated in SF₆-glass PCF by a 1060 nm mode-locked fibre laser delivering 20 pJ per pulse," *Opt. Express* **17**(3), 1919–1924 (2009).
18. C.-H. Li, G. Q. Chang, A. G. Glenday, N. Langellier, A. Zibrov, D. F. Phillips, F. X. Kärtner, A. Szentgyorgyi, and R. L. Walsworth, "Conjugate Fabry-Perot cavity pair for improved astro-comb accuracy," *Opt. Lett.* **37**(15), 3090–3092 (2012).
19. H.-W. Chen, G. Chang, S. Xu, Z. Yang, and F. X. Kärtner, "3 GHz, fundamentally mode-locked, femtosecond Yb-fiber laser," *Opt. Lett.* **37**(17), 3522–3524 (2012).

1. Introduction

Recent years have seen growing efforts to optimize femtosecond-laser frequency combs for astrophysical spectrograph wavelength calibration ("astro-combs") [1–13]. Astro-combs hold promise to provide long-term stability and increased accuracy for astrophysical spectrograph calibration, with applications such as identifying Earth-like exoplanets using stellar Doppler shift spectroscopy to measure periodic exoplanet-induced variations in the stellar radial velocity (RV). At present, astro-combs consist of at least two essential components: a frequency-stabilized source-comb with relatively small spectral line-spacing ($\leq 1 \text{ GHz}$) and a mode-filtering Fabry-Perot (FP) cavity to increase the line spacing to $>10 \text{ GHz}$ by rejecting unwanted spectral lines (referred to as "side modes"), so that the resulting astro-comb lines are resolved by an astrophysical spectrograph (typical resolution $R = \lambda/\Delta\lambda = 10,000\text{--}100,000$).

The bandwidth of an astro-comb is primarily limited by dispersion in the FP filtering cavity from the cavity mirrors and intra-cavity air. Dispersion leads to a mismatch between the cavity's wavelength-dependent free-spectral-range (FSR) and the source-comb's equally spaced comb-lines, resulting in a narrowing of the astro-comb spectral width. Recently we proposed a broadband FP filtering cavity design based on a complementary chirped-mirror pair, and demonstrated in a proof-of-principle experiment a $\sim 40 \text{ GHz}$ filtering cavity with 100 nm bandwidth for a green astro-comb (480–580 nm) [14]. However, implementation of a fully broadband ($>300 \text{ nm}$) astro-comb via direct FP-cavity filtering (Fig. 1(a)) remains extremely challenging. An alternate technique (Fig. 1(b)) is to filter a narrowband source-comb with one

or more narrowband FP cavities, amplify the filtered comb signal, and then produce broadband coverage via subsequent nonlinear spectral broadening in an optical fiber [5,8,11,12]. Such nonlinear spectral broadening arises in an optical fiber from four-wave-mixing cascades among the equally-spaced comb lines, and causes a power redistribution that effectively amplifies both spectral ends of the narrowband spectrum, extending the spectral coverage. Theoretical analysis [5] and experimental measurements [8,12] have shown that such spectral broadening is accompanied by degradation of the side mode suppression, as well as increased imbalance of side modes on opposite sides of each main astro-comb line. (Fig. 2 provides a schematic illustration.)

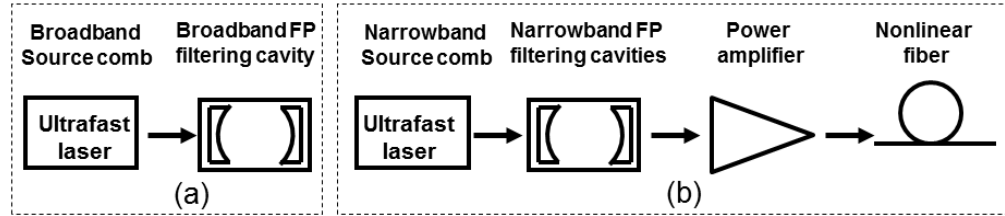


Fig. 1. Schematics of two alternate broadband astro-comb designs: (a) a broadband source-comb is filtered by a broadband FP filter cavity; and (b) a narrowband source-comb is filtered by narrowband FP filter cavities, amplified, and then spectrally broadened in a nonlinear fiber.

The accuracy of astrophysical spectrograph wavelength calibration depends upon minimizing both the intensity of astro-comb side modes (*i.e.*, unwanted source comb spectral lines suppressed by the FP cavity) and their imbalance with respect to the nearest main astro-comb lines (see Fig. 2). In particular, an astrophysical spectrograph with typical resolving power ($R \sim 10,000$ - $100,000$) cannot resolve individual source comb modes. The spectrograph only recovers the center-of-gravity (COG) frequency (or wavelength) of each astro-comb spectral line including the effect of side modes (Fig. 2(c)), which can be approximated as a power-weighted sum of astro-comb lines and their neighboring side modes as

$$v_{COG} \approx v_{astro-comb} + f_{rs} \left[\sum_{k=1}^m k \Re(kf_{rs}) (P_k^u - P_k^l) \right] / [P_0 + \Re(kf_{rs}) \sum_{k=1}^m (P_k^u + P_k^l)], \quad (1)$$

where $v_{astro-comb}$ and P_0 denote the main astro-comb lines' optical frequency and power; f_{rs} is the source-comb's line spacing; and P_k^u (P_k^l) represents the power of the upper (lower) k^{th} side-mode — the unwanted spectral lines that are $k \times f_{rs}$ above (“upper k^{th} side-mode”) and below (“lower j^{th} side-mode”) their associated astro-comb line in the frequency domain. The integer $m \sim R_s / f_{rs}$ is determined by the spectrograph's resolution, R_s , and the source comb's line spacing, f_{rs} . $\Re(f)$ denotes the line profile, *i.e.*, the blue-dashed curve in Fig. 2(c). A shift between the COG frequency and the true astro-comb line frequency generates a systematic calibration error. For studies of stellar radial velocity (RV) variations using Doppler shift spectroscopy, this systematic calibration error (and associated drifts) limits the spectrograph's RV accuracy (and long-term stability) as follows:

$$\Delta RV = c \frac{v_{COG} - v_{astro-comb}}{v_{astro-comb}} \approx c \frac{f_{rs}}{v_{astro-comb}} \left[\sum_{k=1}^m j \Re(kf_{rs}) (P_k^u - P_k^l) \right] / [P_0 + \Re(kf_{rs}) \sum_{k=1}^m (P_k^u + P_k^l)], \quad (2)$$

where c is the speed of light. Studies of rocky, Earth-like exoplanets require <10 -cm/s accuracy and long-term stability of stellar RV measurements, corresponding to an optical frequency accuracy and stability below 200 kHz. For a typical source-comb line spacing of

200 MHz, this requirement translates to $(P_k^u - P_k^l)/P_0 < 10^{-3}$ for the nearest side modes and additional suppression for $k > 1$.

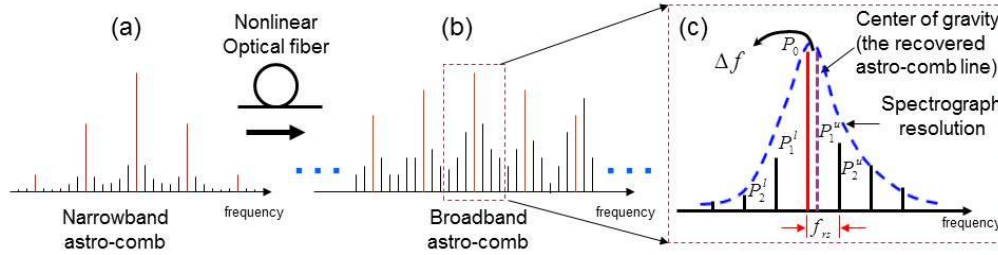


Fig. 2. Nonlinear fiber-optic spectral broadening of a narrowband astro-comb degrades side-mode suppression and causes side-mode amplitude asymmetry, which translate into wavelength calibration error. (a) Narrowband astro-comb generated by filtering a source-comb with one or more narrowband FP cavities. Red, solid lines denote the desired astro-comb lines. Side modes, unwanted, partially suppressed source-comb lines, exist due to the finite suppression of the FP filtering; (b) Broadband astro-comb after nonlinear spectral broadening inside an optical fiber. Cascade four-wave-mixing degrades side-mode suppression and causes side-mode amplitude asymmetry; (c) When used for calibrating astrophysical spectrographs, the broadband astro-comb in (b) generates systematic calibration error. See the text for a detailed discussion.

Following the FP filter cavities, which increase the comb line spacing by M , the comb pulse energy is reduced by a factor of M^2 relative to the source-comb pulse energy. M is typically in the range of 10-100, leading to comb pulse energies in the range of 0.1-1 pJ for current fiber (source-comb) lasers. Extension of the spectral coverage or wavelength shifting of the filtered comb spectrum relies on nonlinear processes inside an optical fiber or crystal, which typically require pulse energies ~ 100 pJ. Thus, power amplification of the filtered narrowband comb is required to boost the pulse energy before nonlinear spectral broadening/conversion. When fiber amplifiers are employed, nonlinear phase accumulates inside the gain medium (*i.e.*, active fiber), which initiates cascaded four-wave-mixing. This process, as discussed above in the context of nonlinear spectral broadening, may dramatically degrade side-mode suppression, systematically shift the COG frequency of astro-comb spectral lines, and thus lead to wavelength calibration error [5,8]. In this paper we theoretically investigate the interplay of FP cavity filtering with power amplification and nonlinear broadening to optimize astro-comb performance in terms of minimizing RV calibration error. The paper is organized as follows: section 2 describes a general astro-comb system. Section 3 provides an outline of the analytical approach to modeling FP cavity filtering and CPA fiber amplification with results presented in section 4. We devote section 5 to numerical modeling of the interplay between four filtering schemes and nonlinear spectral broadening. Finally section 6 concludes the paper.

2. Astro-comb system

2.1 Filtering schemes

There are many potential filter cavity designs. Restricting the number of FP filtering cavities to no more than two and constructing them from identical mirrors, still leaves options for choosing the FSR of each cavity to achieve a given multiplication of line spacing. For two filtering cavities with FSR set as $f_{FSR1} = M_1 f_{rs}$ and $f_{FSR2} = M_2 f_{rs}$, the transmission of these cascade cavities results in an increase of comb spacing by a factor of $M = M_1 M_2$ if M_1 and M_2 are co-prime with each other. Any two FP filtering cavities with $f_{FSR1} = M f_{rs}$ and $f_{FSR2} = (M/N) f_{rs}$ (M and N are co-prime) will lead to M -times comb-spacing multiplication as well; hereafter, we refer to such designs as *fraction-prime* cavities. A special case is for N

= 1, corresponding to a cascade of two identical FP filtering cavities. While these schemes all give rise to the same astro-comb line spacing, they exhibit different magnitudes of side-mode suppression as well as different side-mode phases and thus different sensitivities to four wave mixing and side-mode suppression degradation.

In section 4, we will compare 7 filtering schemes as listed in Table 1: (1) one FP cavity; (2) two identical FP cavities with cavity 2 placed *after* the amplifier; (3) two identical FP cavities with both cavities placed *before* the amplifier; (4) co-prime FP cavities with cavity 2 *after* the amplifier; (5) co-prime FP cavities with both cavities *before* the amplifier; (6) fraction-prime FP cavities with cavity 2 *after* the amplifier; and (7) fraction-prime FP cavities with both cavities *before* the amplifier.

Table 1. Seven Filtering Schemes Compared in this Paper. FPC: Fabry-Perot Cavity; CPA: Chirped-pulse Amplification

Scheme #	Configuration
1	Source-comb→FPC1→CPA amplifier
2	Source-comb→FPC1→CPA amplifier →FPC2 (FPC1 and FPC2 <i>identical</i>)
3	Source-comb→FPC1→FPC2→CPA amplifier (FPC1 and FPC2 <i>identical</i>)
4	Source-comb→FPC1→CPA amplifier →FPC2 (FPC1 and FPC2 <i>co-prime</i>)
5	Source-comb→FPC1→FPC2→CPA amplifier (FPC1 and FPC2 <i>co-prime</i>)
6	Source-comb→FPC1→CPA amplifier →FPC2 (FPC1 and FPC2 <i>fraction-prime</i>)
7	Source-comb→FPC1→FPC2→CPA amplifier (FPC1 and FPC2 <i>fraction-prime</i>)

2.2 Fiber chirped-pulse amplification

Current astro-combs are based on three different laser systems: Ti:sapphire laser [2,4,7,9], Yb-doped fiber laser [3,6,11,12], and Er-doped fiber laser [8,10,13]. We restrict our discussion to fiber-laser based astro-combs since fiber amplifiers provide large (~30 dB) single-pass gain, and fiber lasers promise compactness and robustness. To reduce the detrimental effects of nonlinear phase accumulated inside the fiber amplifier, chirped-pulse amplification (CPA) is exploited, in which the input pulse is stretched, amplified, and finally compressed close to its original duration. The nonlinear phase produced by a CPA system is usually quantified by the B -integral [15], expressed as $B \approx \gamma P_{amp} / g$, where g , γ and P_{amp} denote the small-signal gain coefficient of the amplifier, the nonlinear parameter, and the peak power of the amplified astro-comb pulse, respectively. For a 200 pJ amplified pulse pre-stretched to 10 (or 2) ps, $B \approx 0.12$ (or 0.6) for the typical values of a fiber amplifier: $\gamma = 6/\text{W/km}$ and $g = 1/\text{m}$.

For a traditional ultrafast amplifier, the seed into the amplifier is a train of identical pulses (*i.e.*, constant pulse envelope and peak power), and the amplified pulses remain identical regardless of the magnitude of the nonlinear phase. In this scenario, the B -integral is a good indicator of how well the amplified pulses can be re-compressed to their original duration; a B -integral < 1 indicates minimal effects of nonlinearities inside the fiber amplifier.

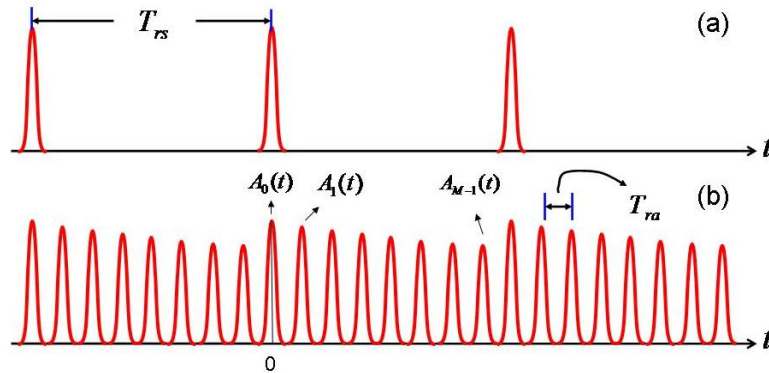


Fig. 3. Pulse repetition-rate multiplication by a FP filtering cavity begins with (a) a train of identical pulses. (b) After the FP cavity, a temporally modulated, high repetition rate pulse train is produced. In this example, $T_{rs} = 8T_{ra}$, *i.e.*, $M = 8$, and the finesse of the FP filter cavity $F = 100$. $A_0(t), A_1(t) \dots A_{M-1}(t)$ denote the amplitudes of M pulses within one modulation period.

In an astro-comb, the input to the amplifier is a pulse train generated from an FP filtering cavity. The FP cavity increases the source-comb line spacing by a factor of M in the frequency domain, which in the time domain multiplies the source-comb's repetition rate by a factor of M . Finite side-mode suppression in the frequency domain of the filtered comb corresponds to a periodic amplitude modulation of the multiplexed pulse train in the time domain (Fig. 3). Since nonlinearity in a fiber amplifier depends on peak pulse power, pulses within one modulation period acquire differing nonlinear phases during amplification. Our calculation in the following sections will show that side-mode suppression is highly susceptible to the nonlinear effects arising from amplifying such a modulated pulse train (Fig. 3(b)).

3. Analytic modeling

3.1 General modeling procedure

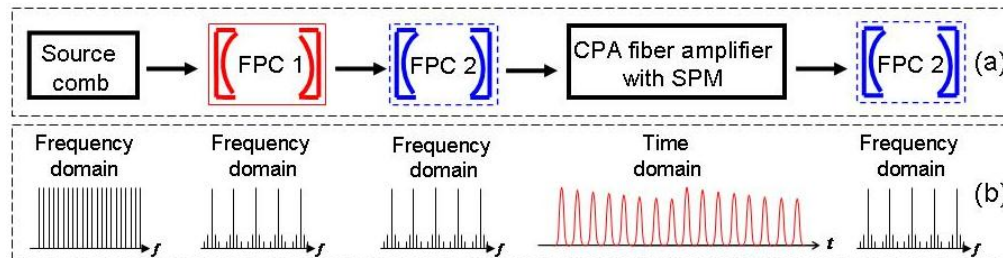


Fig. 4. Schematic representation of analytic model of astro-comb spectral filtering and power amplification. (a) Two sequential arrangements for mode-filtering and power amplification with the second Fabry-Perot Cavity (FPC 2) either before or after the fiber amplifier. (b) Modeling of source-comb, FPC, and amplifier in frequency or time domain. CPA: chirped-pulse amplification; SPM: self-phase modulation.

To study and optimize mode filtering with FP cavities and power amplification, we model two key devices and their interaction: 1) the FP filtering cavity and 2) the CPA fiber amplifier. An FP filtering cavity constructed from two identical mirrors is most easily modeled in the frequency domain. Rigorously modeling a CPA fiber amplifier fed by a train of modulated pulses rigorously, requires numerically solving the generalized nonlinear Schrödinger equation in the time domain using the method developed in Ref. [5]. However numerical modeling is time consuming and often obscures the underlying physics. Given that the narrowband filtering cavity (10 – 30 nm bandwidth) limits the transform-limited pulse

duration to be >100 fs for the pulses seeding the fiber amplifier, higher-order (>2) dispersion and nonlinear effects except for self-phase-modulation (SPM) are negligible to first order. In this scenario, a CPA fiber amplifier can be modeled approximately using analytic techniques [16].

Figure 4 illustrates a block diagram of the astro-comb systems we study, and the corresponding frequency- or time-domain modeling of each element (Fig. 4(b)). In general, analytic modeling of the astro-comb system in Fig. 4(a) includes the following steps:

- (1) *Source-comb*. The spectrum of the source comb with a uniform line spacing of $\omega_{rs} = 2\pi f_{rs}$ (where f_{rs} is the source-comb repetition rate) is modeled in the frequency domain as

$$\tilde{A}_s(\omega) = \tilde{A}_0(\omega) \sum_{l=-\infty}^{+\infty} \delta(\omega - l\omega_{rs}). \quad (3)$$

$\tilde{A}_0(\omega)$ denotes the spectral envelope, $\delta(\omega)$ is the Kronecker delta function: $\delta(\omega) = 1$ for $\omega = 0$ and $\delta(\omega) = 0$ for $\omega \neq 0$, and $\sum_{l=-\infty}^{+\infty} \delta(\omega - l\omega_{rs})$ indicates that nonzero spectral components exist only at discrete angular frequencies: $0, \pm\omega_{rs}, \pm 2\omega_{rs}, \dots, \omega_{rs} = 2\pi f_{rs}$. In Eq. (3), we have centered the spectrum at zero angular frequency.

- (2) *FP filtering cavity*. An FP filtering cavity constructed from two identical mirrors is described in the frequency domain by its transmission function, which connects the output with the input as

$$\frac{E_{out}}{E_{in}} = \frac{(1-R)e^{-j\phi/2}}{1-R \times e^{-j\phi}}. \quad (4)$$

R denotes the mirror reflectivity and ϕ is the cavity round-trip phase. For the filtering of a narrowband source-comb (e.g., bandwidth <30 nm at 1060 nm), dispersion from cavity mirrors and air is negligible, leading to $\phi = 2\omega d / c$, where d is the cavity length. For simplicity, we rewrite Eq. (4) by absorbing the phase $e^{-j\phi/2}$ into E_{in} , and define the amplitude transmission coefficient, t_{FP} , as

$$t_{FP} = \frac{E_{out}}{E_{in} e^{-j\phi/2}} = \frac{1-R}{1-R \times e^{-j\phi}} = \frac{1-R}{\sqrt{1-2R \cos \phi + R^2}} e^{j\varphi}. \quad (5)$$

$\varphi = \tan^{-1}(-R \sin \phi / (1-R \cos \phi))$ is the transmission phase. Replacing E_{in} by $E_{in} e^{-j\phi/2}$ corresponds to a constant temporal delay of the input source-comb pulse train and has no effect on the output astro-comb power spectrum. We note that two identical FP filtering cavities of transmission t_{FP} have a net amplitude transmission of $t_{FP} \times t_{FP}$.

- (3) *Filtered source-comb*. We transform the filtered source-comb spectrum into the time domain to obtain the modulated pulse train. The envelopes of the M pulses within one modulation period are represented by $A_0(t), A_1(t), \dots, A_{M-1}(t)$. These pulses serve as seeds to the CPA fiber amplifier.

(4) *CPA fiber amplifier with SPM.* Modeling the amplifier requires two steps: (i) linear pulse stretching and (ii) power amplification. We summarize the detailed derivation found in Ref. [16]:

(i) *Pulse stretching.* For a pulse of envelope $A_i(t)$ ($i = 0 \dots M-1$), we Fourier transform the pulse to obtain the corresponding spectrum $\tilde{A}_i(\omega)$, and then stretch the pulse by applying a quadratic phase, $\phi_{str} \omega^2/2$. This leads to a spectrum for the stretched pulse of $\tilde{A}_i^{str}(\omega) = \tilde{A}_i(\omega) \exp(j \frac{\phi_{str}}{2} \omega^2)$. Using the method of stationary phase, we found the time-domain stretched pulse envelope, $A_i^{str}(t)$, to be

$$A_i^{str}(t) = \frac{1}{\sqrt{-i 2\pi |\phi_{str}|}} \exp(-j \frac{t^2}{2\phi_{str}}) \tilde{A}_i(\frac{t}{\phi_{str}}).$$

(ii) *Power amplification with SPM.* The stretched pulse experiences amplification and SPM inside the fiber with an output pulse envelope, $A_i^{amp}(t)$, given by $A_i^{amp}(t) = A_i^{str}(t) \exp(\frac{gL}{2}) \exp(j \gamma L_{eff} |A_i^{str}(t)|^2)$, where g , L , and γ denote the gain coefficient, fiber length, and nonlinear coefficient of the amplifier, respectively. L_{eff} is the effective fiber length defined as $L_{eff} = (\exp(gL) - 1) / g$. Again employing the method of stationary phase, we find the optical spectrum for the amplified pulse to be

$$\tilde{A}_i^{amp}(\omega) = \exp(\frac{gL}{2}) \tilde{A}_i(\omega) \exp(j \frac{\phi_{str}}{2} \omega^2) \exp(j B_i s_i(\omega)), \quad (6)$$

where $B_i = \gamma L_{eff} \max |A_i^{str}(t)|^2$ and $s_i(\omega) = |\tilde{A}_i(\omega)|^2 / \max |\tilde{A}_i(\omega)|^2$ is the normalized spectrum.

(5) From step (4), we can find the amplified spectrum of each individual pulse. Summing the output pulses of envelopes $\tilde{A}_0(t), \tilde{A}_1(t) \dots \tilde{A}_{M-1}(t)$ results in the spectrum of the amplified astro-comb:

$$\tilde{A}^{amp}(\omega) = \left[\tilde{A}_0^{amp}(\omega) + \tilde{A}_1^{amp}(\omega) e^{-j\omega T_m} + \dots + \tilde{A}_{M-1}^{amp}(\omega) e^{-j\omega(M-1)T_m} \right] \sum_{l=-\infty}^{+\infty} \delta(\omega - l \omega_{rs}), \quad (7)$$

where $T_m = 1 / (M f_{rs})$, is the temporal separation between two adjacent pulses in the modulated pulse train. A second, identical FP filtering cavity after the amplifier, results in a filtered spectrum given by $\tilde{A}^{amp}(\omega) \times t_{FP}$.

3.2 Analytic modeling results for the schemes listed in Table 1

Appendices at the end of this paper provide a derivation of the output spectra for the amplified high repetition-rate astro-combs using the seven schemes listed in Table 1. These are summarized as follows:

Scheme 1—A single FP filtering cavity followed by the CPA fiber amplifier. The FP cavity has an FSR satisfying $f_{FSR} = M f_{rs}$ where f_{rs} is the source-comb's spectral line spacing (*i.e.*, the repetition rate of the source-comb laser). The simplified output spectrum is given by Eq. (A7) in Appendix A:

$$\tilde{A}^1(\omega) = \left\{ \sum_{m=0}^{M-1} R^m \exp[-j\omega m T_{ra} + jR^{2m} B_{1,0} s_0(\omega)] \right\} \tilde{A}_0(\omega) \sum_{l=-\infty}^{+\infty} \delta(\omega - l\omega_{rs}),$$

where R is the mirror reflectivity, T_{ra} is the time between astro-comb pulses, $B_{1,0} = \gamma L_{eff} \max \left[|A_0^{sr}(t)|^2 \right]$ is a constant determined from the B integral of the first pulse emitted from the cavity after stretching in the CPA, and $s_0(\omega) = |\tilde{A}_0(\omega)|^2 / \max |\tilde{A}_0(\omega)|^2$ is the normalized spectrum of the first pulse.

Scheme 2—Two identical FP filtering cavities with the CPA fiber amplifier placed between the two cavities. Both FP cavities have an FSR satisfying $f_{FSR} = Mf_{rs}$. The simplified output spectrum is given by Eq. (B1) in Appendix B:

$$\tilde{A}^2(\omega) = \frac{1-R}{1-e^{-j\omega T_{ra}} R} \left\{ \sum_{m=0}^{M-1} R^m \exp[-j\omega m T_{ra} + jR^{2m} B_{1,0} s_0(\omega)] \right\} \tilde{A}_0(\omega) \sum_{l=-\infty}^{+\infty} \delta(\omega - l\omega_{rs}).$$

Scheme 3—Two identical FP filtering cavities followed by the CPA fiber amplifier and both FP cavities have $f_{FSR} = Mf_{rs}$. The simplified output spectrum is given by Eq. (C6) in Appendix C:

$$\tilde{A}^3(\omega) = \left\{ \sum_{m=0}^{M-1} \rho_m R^m \exp[-j\omega m T_{ra} + j\rho_m^2 R^{2m} B_{3,0} s_0(\omega)] \right\} \tilde{A}_0(\omega) \sum_{l=-\infty}^{+\infty} \delta(\omega - l\omega_{rs}),$$

where $\rho_m = m+1+(M-m-1)R^M$, $m=0,1,\dots,M-1$.

Scheme 4—Two co-prime FP filtering cavities with the CPA fiber amplifier between the cavities. The FP cavities have FSR satisfying $f_{FSR1} = M_1 f_{rs}$ and $f_{FSR2} = M_2 f_{rs}$, where M_1 and M_2 are co-prime and $M = M_1 M_2$. The simplified output spectrum is given by Eq. (D2) in Appendix D:

$$\tilde{A}^4(\omega) = \frac{1-R}{1-e^{-j\omega T_{ra}/M} R} \left\{ \sum_{m=0}^{M_1-1} R^m \exp[-j\omega m T_{ra} + jR^{2m} B_{4,0} s_0(\omega)] \right\} \tilde{A}_0(\omega) \sum_{l=-\infty}^{+\infty} \delta(\omega - l\omega_{rs}).$$

Scheme 5—Two co-prime FP filtering cavities followed by the CPA fiber amplifier. The FP cavities have FSR $f_{FSR1} = M_1 f_{rs}$ and $f_{FSR2} = M_2 f_{rs}$, where M_1 and M_2 are co-prime and $M = M_1 M_2$. The simplified output spectrum is given by Eq. (E4) in Appendix E:

$$\tilde{A}^5(\omega) = \left\{ \sum_{m=0}^{M-1} R^{p(m)} \exp[-j\omega m T_{ra} + jR^{2p(m)} B_{5,0} s_0(\omega)] \right\} \tilde{A}_0(\omega) \sum_{l=-\infty}^{+\infty} \delta(\omega - l\omega_{rs}),$$

where $p(m) = n+k$ with $\text{mod}(M_2 n + M_1 k, M) = m$, and $n, k = 0, 1, \dots, M-1$.

Scheme 6—Two fraction-prime FP filtering cavities with the CPA fiber amplifier between the cavities. These FP cavities have FSR $f_{FSR1} = Mf_{rs}$ and $f_{FSR2} = (M/N)f_{rs}$, where M and N are co-prime. The simplified output spectrum is given by Eq. (F1) in Appendix F:

$$\tilde{A}^6(\omega) = \frac{1-R}{1-e^{-j\omega T_{ra} N/M} R} \left\{ \sum_{m=0}^{M-1} R^m \exp[-j\omega m T_{ra} + jR^{2m} B_{6,0} s_0(\omega)] \right\} \tilde{A}_0^s(\omega) \sum_{l=-\infty}^{+\infty} \delta(\omega - l\omega_{rs}).$$

Scheme 7—Two fraction-prime FP filtering cavities followed by the CPA fiber amplifier. The FP cavities have FSR $f_{FSR1} = Mf_{rs}$ and $f_{FSR2} = (M/N)f_{rs}$, with M and N are co-prime. The simplified output spectrum is given by Eq. (G5) in Appendix G:

$$\tilde{A}^7(\omega) = \left\{ \sum_{m=0}^{M-1} \eta(m) \exp[-j\omega m T_{ra} + j\eta(m)B_{7,0}s_0(\omega)] \right\} \tilde{A}_0(\omega) \sum_{l=-\infty}^{+\infty} \delta(\omega - l\omega_{rs}),$$

where $\eta(m) = \sum_{i=0}^m R^{i+f(m-i)} + \sum_{i=m+1}^{M-1} R^{i+f(M+m-i)}$, $f(m) = \text{mod}(mk_0, M)$. Since M and N are co-prime, there exists k_0 such that $0 \leq k_0 \leq M-1$ and $\text{mod}(Nk_0, M) = 1$.

In these equations, $B_{1,0}, B_{3,0}, B_{4,0}, B_{5,0}, B_{6,0}$, and $B_{7,0}$ are constants determined from the B integral of the pulse in the CPA fiber amplifier.

4. Modeling parameters and results for seven filtering schemes

To compare the seven filtering schemes, we assume that all the FP cavities consist of two identical mirrors with 98.8% power reflectivity and the high repetition-rate astro-comb is created by multiplying the source-comb line spacing by a factor of 63. The FSR of each FP cavity is chosen as follows: (1) $f_{FSR} = 63f_{rs}$ for a single FP filtering cavity; (2) $f_{FSR1} = f_{FSR2} = 63f_{rs}$ for two identical FP cavities; (3) $f_{FSR1} = 7f_{rs}$ and $f_{FSR2} = 9f_{rs}$ for co-prime FP cavities; and (4) $f_{FSR1} = 63f_{rs}$ and $f_{FSR2} = (63/8)f_{rs}$ for fraction-prime cavities. We also assume: (1) without loss of generality, the source-comb has a Gaussian spectral envelope; (2) it has a line spacing of 250 MHz—the repetition-rate of Yb-fiber/Er-fiber oscillators employed in current astro-combs; and (3) the source-comb centers at 1.06 μm with a bandwidth of 200 times the astro-comb spacing (*i.e.*, $200 \times 63 \times 250 \text{ MHz} = 3,150,000 \text{ MHz}$). After any of these seven filtering schemes, each pulse from the source-comb generates 63 pulses with differing pulse energies. To make a fair comparison, the pulse energy of the strongest of the 63 pulses is chosen to be the same for all the seven schemes. This is equivalent to enforcing

$$\max(R^{2m})B_{1,0} = \max(\rho_m^2 R^{2m})B_{3,0} = \max(R^{2m})B_{4,0} / M_2^2 = \max(R^{2p(m)})B_{5,0} = \max(R^{2m})B_{6,0} = \max(\eta(m))B_{7,0} \equiv B_{eff},$$

where B_{eff} is the effective B-integral. Note that in scheme 4, the 2nd FP cavity reduces the pulse energy by M_2^2 , and hence the amplifier placed before the 2nd FP cavity must amplify the input pulse to an energy M_2^2 times larger than the other schemes, resulting in M_2^2 times larger nonlinear phase. This leads to the appearance of M_2^2 in the above equation for normalizing the pulse energy in cavity scheme 4.

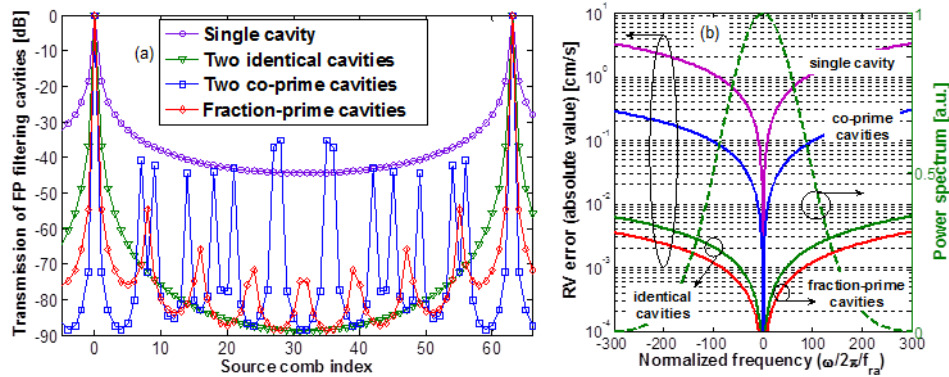


Fig. 5. (a) Transmission of 4 types of FP cavity combinations in the absence of the CPA fiber amplifier: single cavity (purple-circles), identical cavities (green-triangles), co-prime cavities (blue-squares), and fraction-prime cavities (red-diamonds). All the cavities are constructed from two identical mirrors with 98.8% power reflectivity. (Dispersion from mirror coatings and cavity air are neglected.) (b) RV error corresponding to the 4 FP filtering methods. Also shown in (b) is the envelope of the source-comb optical spectrum (green-dashed curve) with a full-width-half-maximum of 200 times the astro-comb spacing.

If the CPA fiber amplifier is absent, the seven filtering schemes for comb-spacing multiplication reduce to four schemes whose power transmission curves are shown in Fig. 5(a): (1) a single FP filtering cavity (purple-circle curve), (2) two identical FP cavities (green-triangle curve), (3) two co-prime FP cavities (blue-square curve), and (4) two fraction-prime FP cavities (red-diamond curve). Dispersion from mirror coatings and cavity air are neglected in the calculations performed to produce this figure. While the four filtering schemes all transmit every 63rd source-comb line, they differ in side-mode suppression. Both single cavities and identical cavities exert higher suppression for side modes farther away from their associated astro-comb lines. Co-prime cavities and fraction-prime cavities exhibit suppression oscillation; that is, they suppress lower-order (e.g., 1st-6th) side modes more than identical cavities, while providing less suppression for certain higher-order side modes (e.g., 7th, 9th for the co-prime cavities and 8th for the fraction-prime cavities).

For a given astro-comb line, its upper k^{th} side-mode and lower k^{th} side-mode are equally suppressed in all the four filtering schemes. If the source-comb has a flat spectrum, these side modes have symmetric amplitudes relative to their associated astro-comb lines (i.e., $P_k^u = P_k^l$ in Eq. (2)), preventing RV calibration errors. For a source-comb with a Gaussian spectral envelope, 250 MHz line spacing, and a bandwidth 200 times the astro-comb spacing (i.e., $\text{BW} = 200f_m = 200 \times 63 \times 250 \text{ MHz}$), P_k^u is slightly different from P_k^l . Consequently, calibration errors occur, which can be estimated using Eq. (2). We estimate

these calibration errors assuming a spectrograph line profile $\Re(\nu) = \exp[-(\frac{\nu}{\Delta\nu/1.665})^2]$

with a full width at half maximum of $\Delta\nu = f_m/3$. The calculated RV error as a function of normalized frequency is illustrated in Fig. 5(b) in the absence of fiber amplifiers. Without the CPA, filtering with single cavity or co-prime cavities leads to much larger calibration error than the other two filtering methods. However, even these filtering schemes provide sufficient accuracy for the characterization of exo-Earths across most of their bandwidths in the absence of the nonlinear phase accumulation associated with the fiber amplifier.

For a given astro-comb line, its upper i^{th} and lower i^{th} side modes pick up *opposite* phase shifts from the cavity filter. During nonlinear spectral broadening this *opposite* phase together with four-wave mixing leads to differential amplification of the upper and lower side modes, causing a systematic COG shift of the astro-comb lines and thus leading to

considerable calibration error [5]. Since SPM is a type of four-wave mixing, SPM in the CPA fiber amplifier will also produce systematic shifts in the COG of astro-comb lines due to differential amplification of side modes. In the next 3 subsections, we provide a detailed comparison of the seven filtering schemes under the same nonlinear phase corresponding to $B_{eff} = 0.6$.

4.1 Results for one cavity (scheme 1) or two identical cavities (schemes 2-3)

The power of the first three side modes relative to their associated astro-comb lines is shown for schemes 1-3 in Fig. 6. During amplification, SPM creates amplitude imbalance such that, for scheme 1 (Fig. 6(a)), lower side modes (red-solid lines) become stronger than the upper side modes (blue-dashed lines). This phenomenon is most pronounced in the central region of the spectrum. Using Eq. (2), we find the corresponding RV error, plotted in Fig. 6(d) as the purple curve. Adding a second cavity to scheme 1 produces scheme 2, which exhibits the same magnitude of side-mode imbalance, though with reduced overall power in the side modes (Fig. 6(b)). The reduction in overall side-mode power reduces RV error by two orders of magnitude (red-dashed curve in Fig. 6(d)) compared to scheme 1.

Scheme 3 (two identical cavities followed by a CPA fiber amplifier) further improves performance; the resulting suppression of upper and lower side modes is more balanced, with a suppression difference <0.5 dB (<0.1 dB between the upper and lower 1st side modes; see Fig. 6(c)). Scheme 3 exhibits RV errors <0.01 cm/s (blue-dashed curve in Fig. 6(d)), representing 1-2 orders of magnitude improvement over scheme 2. A comparison of Fig. 6(a) and Fig. 6(c) also reveals that the upper 2nd and 3rd side modes (blue-dashed lines) from scheme 3 exceed their corresponding lower side modes (red-solid lines), unlike scheme 1 for which the lower side modes are always stronger than their upper counterparts.

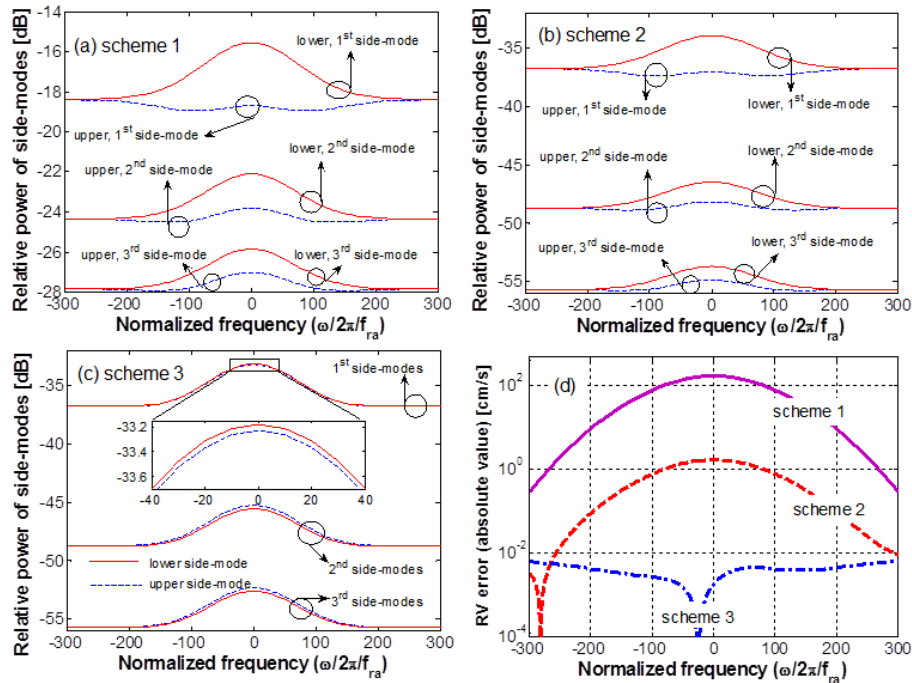


Fig. 6. (a)-(c) Relative power of the first three side modes as a function of normalized frequency for filtering schemes 1-3; Inset on (c) shows a close-up view of the 1st side modes at the spectrum's central region. (d) RV error as a function of normalized frequency for filtering schemes 1-3. (Nonlinear phase for these calculations: $B_{eff} = 0.6$.)

4.2 Results for co-prime FP cavities ($f_{FSR1} = 7f_{rs}$, $f_{FSR2} = 9f_{rs}$) with the amplifier in between the two cavities (scheme 4) or after the 2nd cavity (scheme 5)

In cavity filtering schemes 4 and 5 the 9th and 27th side modes are not strongly suppressed due to the resonance structure of the cavities (see Fig. 5(a)) and thus dominate the RV errors. In scheme 4 (co-prime cavities with the amplifier between the two cavities), only the first cavity contributes to the suppression of the 9th and 27th (and 18th) side modes since they coincide with the transmission peaks of the 2nd FP cavity. These side modes are dramatically and unevenly amplified (Fig. 7(a)) with the upper and lower 27th side modes exhibiting >20 dB suppression difference in the central spectral region of the comb. Also in this spectral region, the upper, 27th side-mode becomes >10 dB (close to 40 dB at some frequencies) stronger than the corresponding astro-comb lines. The resulting RV error reaches as high as 100 cm/s (red-solid curve in Fig. 7(c)).

Suppression of the 9th and 27th side modes is improved in scheme 5, as shown in Fig. 7(b). With filtering by both FP cavities prior to amplification, these side modes are more immune to FWM; the suppression degrades only 3 dB at most, with a <0.5 dB suppression difference between the upper and lower side modes. Thus the resulting RV error is reduced from that of scheme 4 by more than two orders of magnitude, reaching as low as <0.3 cm/s.

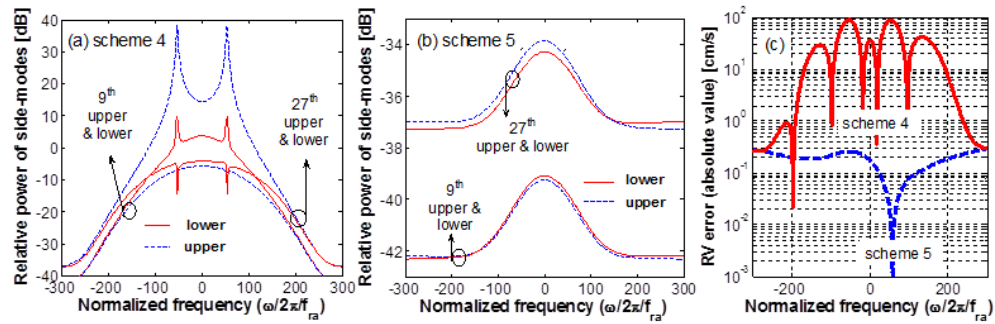


Fig. 7. Relative power of the 9th and 27th side modes as a function of normalized frequency for filtering schemes (a) 4 and (b) 5. (c) RV error as a function of normalized frequency for filtering schemes 4 and 5. (Nonlinear phase for these calculations: $B_{eff} = 0.6$.)

4.3 Results for fraction-prime FP cavities ($f_{FSR1} = 63f_{rs}$, $f_{FSR2} = (63/8)f_{rs}$) with the amplifier before (scheme 6) or after (scheme 7) the 2nd cavity

When filtering with fraction-prime FP cavities, the 1st, 8th, 2nd, and 16th side modes experience poor suppression (red-diamond curve in Fig. 5(a)) and thus dominate the contribution to RV error. The relative power of these side modes as a function of normalized frequency are shown in Fig. 8 for fraction-prime cavities with the amplifier before or after the second cavity.

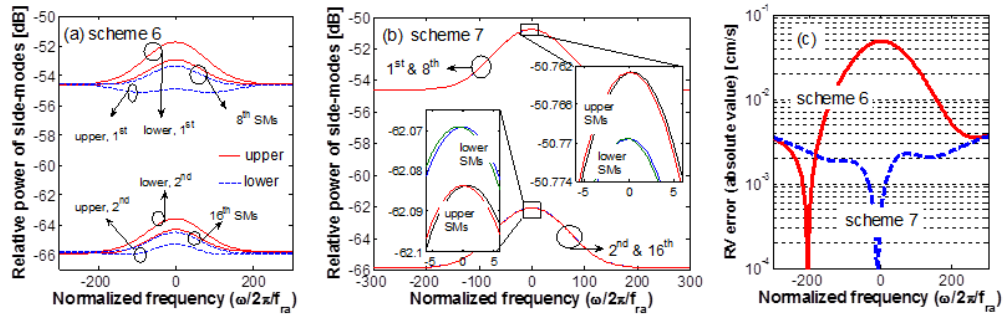


Fig. 8. (a)-(b) Relative power of the 1st, 8th, 2nd, and 16th side modes as a function of normalized frequency for filtering scheme 6 and 7; (c) RV error as a function of normalized frequency for filtering schemes 6 and 7. Nonlinear phase $B_{eff} = 0.6$. SMs: side modes. Insets of (b) show a close-up of the side modes in the spectrum's central region.

A comparison of Fig. 8(a) and Fig. 8(b) reveals that scheme 7 (both fraction-prime FP cavities before the amplifier) results in more balanced side-mode suppression with similar overall rejection. In scheme 7, before amplification, the upper (lower) 1st side modes experience the *same* suppression (red-diamond curve in Fig. 5(a)) and acquire the *same* phase as the upper (lower), 8th side modes do. As a result, after the amplification, these two side modes nearly coincide (red and black curves in the right inset of Fig. 8(b)). The same balancing happens between the 2nd and 16th side modes. In scheme 6 (fraction-prime cavities with the amplifier between the two cavities), the suppression imbalance for these side modes is more substantial (Fig. 8(a)), resulting in an RV error 10 dB worse at the spectrum's central region than can be achieved by scheme 7 (Fig. 8(c)).

Although using large-mode-area Yb-fiber can further mitigate the nonlinear effects, the results of this section reflect a general feature in filter configuration: filtering with two cavities prior to the power amplification (schemes 3, 5, and 7) is more resilient to nonlinear effects and outperforms schemes with the amplifier placed between the two cavities (schemes 2, 4, and 6). It is noteworthy that the small nonlinear phase ($B_{eff} = 0.6$) during amplification induces an RV error for schemes 3, 5, and 7 well below 10-cm/s—the accuracy required for Earth-like exoplanet searches and characterization. Indeed, the RV error associated with these schemes (blue-dashed curves in Fig. 6(b), 7(b), and 8(b)) only deviates slightly from the calculated results in absence of nonlinear effects (blue, green, and red curves in Fig. 5(b)), indicating that nonlinear effects with $B_{eff} < 1$ from the CPA amplifier are negligible for these three schemes.

To achieve broadband wavelength coverage, filtered and amplified narrowband pulses are injected into an optical fiber for nonlinear spectral broadening, which accumulates a nonlinear phase $\gg 1$. Modeling the entire astro-comb system enables us to determine the optimal filtering scheme amongst schemes 3, 5, and 7 including both the CPA and the broadening fiber, as discussed in the next section.

5. Modeling the broadband astro-comb

A broadband astro-comb, as depicted schematically in Fig. 9, consists of three key components: (1) a mode-locked femtosecond laser creating a narrowband source-comb, (2) two filtering cavities followed by a fiber amplifier producing the amplified, narrowband astro-comb, and (3) highly nonlinear fiber which spectrally broadens to achieve the broadband astro-comb. The system parameters we use for modeling the broadband astro-comb are similar to those of section 4: (1) the source-comb has 250-MHz line spacing, is centered at 1.06 μm , and emits a train of hyperbolic-secant pulses with 60 fs duration; (2) two filtering cavities multiply the source-comb line spacing by a factor of 63; and (3) all the FP cavities consist of two identical mirrors with 98.8% power reflectivity. After the amplifier, we

assume the pulses are compressed back to their original 60 fs duration. The 63 pulses in one modulation period have slightly different pulse energy, and their sum can be written in the time domain in the following general form:

$$A_a(t) = \sum_{m=0}^{62} A_m(t) * \delta(t - mT_m). \text{ The derivation in the appendices shows that different}$$

filtering schemes lead to different relative pulse power of the 63 pulses. From appendices C, E, and G, we have $A_m(t) = (\rho_m^2 R^{2m} / \rho_0^2) A_0(t)$, $A_m(t) = (R^{2p(m)} / R^{2p(0)}) A_0(t)$, and $A_m(t) = (\eta(m) / \eta(0)) A_0(t)$ for filtering schemes 3, 5, and 7, respectively. For each filtering scheme, we assume that the strongest pulse amongst the 63 pulses has an energy of 60 pJ at the input of the spectral broadening fiber.

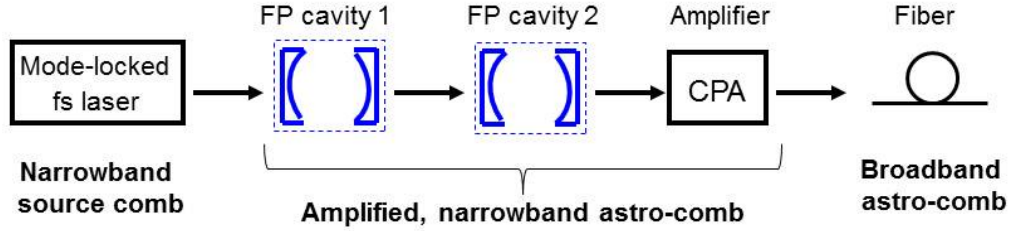


Fig. 9. Schematic of a broadband astro-comb, consisting of three key components: (1) a mode-locked femtosecond laser as the narrowband source-comb, (2) two filtering cavities followed by a fiber amplifier to obtain the amplified, narrowband astro-comb, and (3) highly nonlinear fiber for spectral broadening to achieve the broadband astro-comb.

Spectrally broadening a narrowband source (~ 30 nm) to > 300 nm involves the interaction of many effects (e.g., SPM, self-steepening, stimulated Raman scattering, higher-order dispersion, etc.). This highly nonlinear process may be modeled by the generalized nonlinear Schrödinger (GNLS) equation [15]

$$\frac{\partial A}{\partial z} + \left(\sum_{n=2} \beta_n \frac{i^{n-1}}{n!} \frac{\partial^n}{\partial T^n} \right) A = i\gamma \left(1 + \frac{i}{\omega_0} \frac{\partial}{\partial T} \right) \left(A(z, T) \int_{-\infty}^{+\infty} R(t') |A(z, T - t')|^2 dt' \right),$$

where $A(z, t)$ denotes the pulse's amplitude envelope. β_n , γ , and ω_0 characterize the n^{th} order fiber dispersion, fiber nonlinearity, and pulse center frequency, respectively. $R(t)$ describes both the instantaneous electronic and delayed molecular responses of fused silica, and is defined as

$$R(t) = (1 - f_R) \delta(t) + f_R (\tau_1^2 + \tau_2^2) / (\tau_1 \tau_2^2) \exp(-t / \tau_2) \sin(t / \tau_1),$$

where typical values of f_R , τ_1 , and τ_2 are 0.18, 12.2 fs, and 32 fs, respectively [15]. In the simulation, the fiber's parameters are adapted from Ref.[17] for a 2 cm SF6-glass photonic-crystal fiber (PCF) with 1.7 μm mode-field diameter and nonlinearity of $\gamma = 570 \text{ W}^{-1}\text{km}^{-1}$. The fiber's dispersion is obtained by fitting experimental data (Fig. 2 in Ref. [17]) with a 6th order polynomial. In the simulation, we use the GNLS equation to propagate each of the 63 pulses separately, and then stitch the spectrally-broadened pulses together to determine the comb line intensities in the frequency domain.

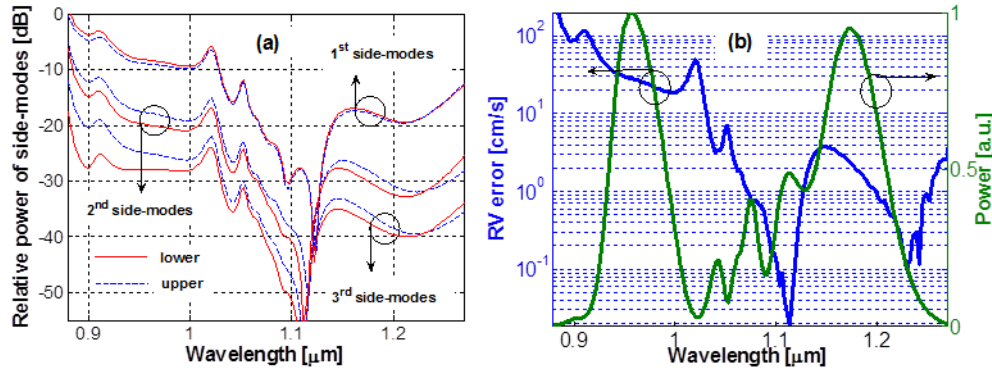


Fig. 10. (a) Relative power of the first three side modes in the broadband astro-comb using filtering scheme 3 (two identical FP cavities followed by a CPA amplifier). (b) RV error as a function of wavelength (blue curve) and the astro-comb spectrum (green curve).

Figure 10 shows the spectrum of a broadband astro-comb generated from filtering scheme 3 (two identical FP cavities followed by a CPA amplifier) feeding a 2 cm SF6 PCF for spectral broadening. The generated broadband astro-comb, (green curve in Fig. 10(b)) has ~ 300 nm bandwidth (width measured at intensities 10 dB below peak) and features two distinct spectral regions of intensity maxima at $0.96 \mu\text{m}$ and $1.17 \mu\text{m}$. Since higher-order dispersion and nonlinear effects beyond SPM play a significant part in spectral broadening in PCF, the wavelength dependence of side modes differs from that determined for the CPA fiber amplifier, in which the side modes are symmetric with respect to the center frequency (or wavelength); see Fig. 6(c) for an example. Figure 10(a) shows the wavelength-dependent relative power of the 1st, 2nd, and 3rd side modes, which are amplified by the four-wave mixing that broadens the astro-comb spectrum. These side modes all show a similar wavelength dependence: they experience ~ 30 dB amplification (*i.e.*, ~ 30 dB degradation of side-mode suppression) between 0.9 and $1 \mu\text{m}$ and ~ 20 dB amplification in the 1.15 - $1.25 \mu\text{m}$ region. The suppression difference between the lower (red curve) and upper (blue-dashed curve) side modes becomes more imbalanced for 0.9 - $1 \mu\text{m}$ than that in the 1.15 - $1.25 \mu\text{m}$ region. Consequently, the resulting RV error (blue-curve in Fig. 10(b)) reaches >20 cm/s in the short wavelength region, while the RV error in the long wavelength region remains <4 cm/s.

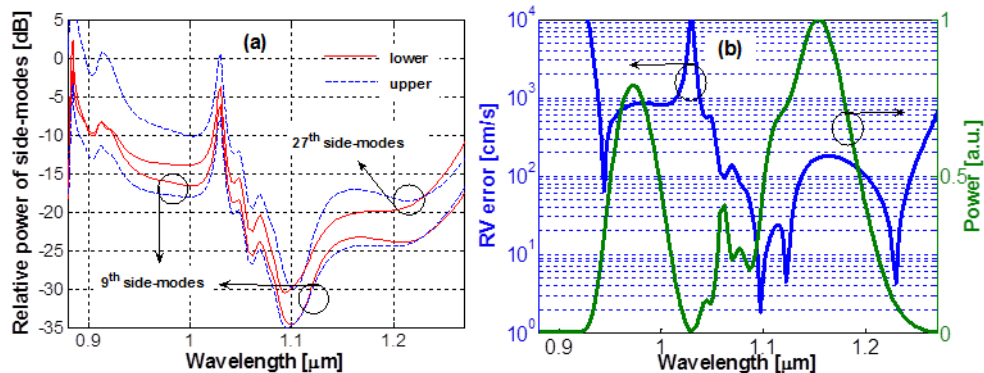


Fig. 11. (a) Relative power of the 9th and 27th side modes in the broadband astro-comb using filtering scheme 5 (two co-prime cavities followed by a CPA amplifier). (b) RV error as a function of wavelength (blue curve) and the astro-comb spectrum (green curve).

Figure 11 summarizes the simulation results for the broadband astro-comb using scheme 5 (two co-prime cavities followed by a CPA amplifier) as the input to the spectral broadening fiber. The most critical side modes for scheme 5, as discussed in Sec. 4.2 are the 9th and 27th, for which the intensity relative to their nearest astro-comb lines are shown in Fig. 11(a). Large imbalances in these side modes lead to RV errors as high as 1000 cm/s at the short wavelength range and 100 cm/s at the long wavelength range (Fig. 11(b)). This RV error is >20 times larger than for filtering scheme 3 (two identical FP cavities followed by a CPA amplifier, see Fig. 10(b)), confirming that filtering with co-prime cavities is more susceptible to fiber nonlinearity.

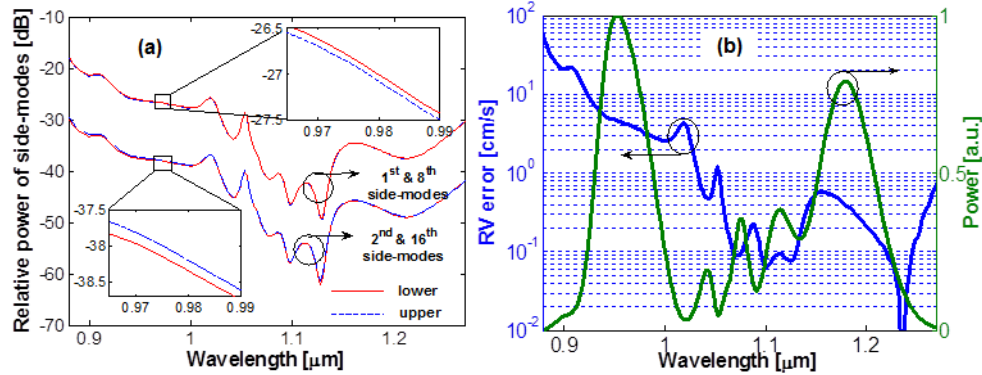


Fig. 12. (a) Relative power of the 1st, 2nd, 8th, and 16th side modes in the broadband astro-comb using filtering scheme 7 (two fraction-prime cavities followed by a CPA amplifier). (b) RV error as a function of wavelength (blue curve) and the astro-comb spectrum (green curve). Insets of (a) show an expanded view of the side modes at the spectral region corresponding to the left peak of the astro-comb spectrum (green curve in (b)).

Figure 12 shows the spectrum of a broadband astro-comb generated from filtering scheme 7 (two fraction-prime cavities followed by a CPA amplifier) followed by spectral broadening. The least filtered side modes of the fraction-prime cavities are the 1st, 2nd, 8th, and 16th (Fig. 5(a)). Figure 12(a) shows the wavelength-dependent relative power of these side modes, which exhibit much smaller power distribution imbalance (<0.2 dB, see the insets in Fig. 12(a)) between the upper and lower side modes than those of the previous filtering schemes. Such minimal imbalance leads to <10 cm/s RV error over the spectra range of 0.92-1.27 μm , as shown in Fig. 12(b).

As we discussed in section 4, the upper and lower i^{th} side modes for a given astro-comb line acquire *opposite* phase shifts from these cavity-filtering schemes. During the subsequent nonlinear spectral broadening inside the PCF, these *opposite* phases lead to differential amplification of the upper and lower side modes during the four-wave mixing process in the PCF, causing a power distribution imbalance and RV error. Ideal filtering, therefore, should introduce no (or identical) phase shifts to the filtered comb lines. Fortunately, a special case of fraction-prime cavities, referred to as conjugate Fabry-Perot Cavities [18] lead to zero phase shifts for the side modes of the astro-comb lines. As we defined in section 2.1, two FP filtering cavities with $f_{FSR1} = Mf_{rs}$ and $f_{FSR2} = (M/N)f_{rs}$ (M and N are co-prime) comprise a fraction-prime cavity pair. One special case is where $N = M-1$. The transmission from these two cavities at the comb frequency mf_{rs} (m is an integer) is $t_{FP1} = (1-R)/(1-R^{-j2\pi m/M})$ and $t_{FP2} = (1-R)/[1-R^{-j2\pi m(M-1)/M}]$, respectively. The overall transmission of the two cavities is then given by

$$t_{FP1}t_{FP2} = (1-R)^2 / [1 - 2R \cos(2\pi q / M) + R^2] = |t_{FP1}|^2. \quad (8)$$

For all source-comb lines, the transmission amplitudes of both cavities are equal while the phases are opposite. Thus the response of the second cavity is conjugate to the first cavity as shown in Eq. (8). Unlike previously described filtering schemes, the conjugate cavities impart no extra phase to the filtered side modes. We expect that such an intriguing characteristic would minimize the upper-lower side-mode power imbalance and thus reduce the RV error.

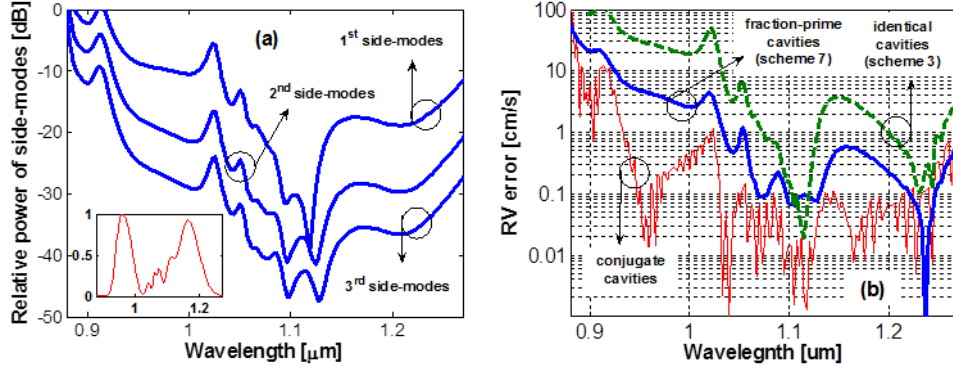


Fig. 13. (a) Relative power of the first three side modes in the broadband astro-comb using conjugate FP cavities for filtering (two conjugate FP cavities followed by a CPA amplifier); inset: astro-comb spectrum. (b) RV error as a function of wavelength for three filtering schemes: identical cavities (green-dashed), fraction-prime cavities (blue), and conjugate cavities (red).

Figure 13 illustrates the simulation results for the broadband astro-comb that employs conjugate cavities ($f_{FSR1} = 63 \times 250$ MHz and $f_{FSR2} = (63/62) \times 250$ MHz) followed by a CPA amplifier to generate the input to the spectral broadening fiber. Figure 13(a) shows the wavelength-dependent relative power of the 1st, 2nd, and 3rd side modes, whose upper-lower side mode imbalance becomes indistinguishable (indeed, <0.005 dB). The *transmission amplitude* of this conjugate cavity pair is equal to the transmission of the identical cavities with $f_{FSR1} = f_{FSR2} = 63 \times 250$ MHz (Eq. (8)). The difference between two identical cavities and two conjugate cavities is that the conjugate cavities impart no phase shift to filtered side modes while identical cavities impose discrete, opposite phase shifts. A comparison between Fig. 13(a) and Fig. 10(a) confirms that such phase-shift differences lead to more balanced side mode power distribution for the broadened astro-comb incorporating conjugate cavities. The RV error for three filtering schemes: identical cavities (green-dashed curve), fraction-prime cavities (blue), and conjugate cavities (red) is plotted in Fig. 13(b). Filtering with conjugate cavities reduces the RV error below that of the other schemes presented here, reaching <1 cm/s with >300 nm wavelength coverage in 0.92 - 1.27 μm .

6. Discussion and conclusion

Implementing a broadband (~ 300 nm) astro-comb from a narrow band, fiber-laser-based source-comb demands two subsequent steps: (1) narrowband cavity filtering and power amplification, and (2) spectral broadening in a highly nonlinear fiber. In this paper, we analyzed the effect of filtering schemes on the astro-comb performance in these two steps. For step 1, which employs a CPA fiber amplifier featuring nonlinear phase $B_{eff} < 1$, we analytically studied seven filtering schemes, all of which increase the comb spacing by a factor of 63 while suppressing side modes differently. We found that the small nonlinear phase introduced by the CPA can aggravate side-mode suppression and introduce side-mode amplitude imbalance, resulting in RV error for spectrograph calibration. We also found that, in general, filtering with two cavities *prior to* the CPA fiber amplifier produces less RV error compared to placing the amplifier between the two cavities.

We also numerically investigated the effect of double cavity filtering on the spectral broadening in step 2 for nonlinear phase $B_{eff} \gg 1$. Four filtering schemes—*identical*, *co-prime*, *fraction-prime*, and *conjugate cavities* characterized by the relation between the two cavities' FSR—were compared in terms of side mode suppression and the resulting RV calibration error. The results shown in Figs. 10–13 reveal some common features shared by these four filtering methods: (1) side modes experience larger suppression degradation (~ 30 dB) at short wavelengths (0.9–1 μm); (2) the side-mode power imbalance is also more severe in the short wavelength range; and (3) consequently, the resulting RV error in the short wavelength region appears ~ 5 times larger than that in the long wavelength region (1.15–1.25 μm). While filtering with co-prime cavities and identical cavities does not provide 300 nm bandwidth of high accuracy calibration light, the other two schemes (*fraction-prime* cavities and *conjugate* cavities) are able to provide >300 nm wavelength coverage in which the RV error <10 cm/s requirement is fulfilled, enabling calibration of astrophysical spectrographs for use in the search for and characterization of Earth-like extra-solar planets. In particular, the conjugate cavity design is the least sensitive to nonlinearities due to the absence of phase shifts on the astro-comb side modes, and leads to RV error < 1 cm/s in the 0.92–1.27 μm spectral band.

It is noteworthy that we have assumed 250-MHz source-comb spacing in our entire analysis. Using a source-comb with higher line spacing will benefit the astro-comb construction by reducing system complicity and calibration RV error. Recently, we have demonstrated a fundamentally mode-locked, femtosecond (~ 206 fs) Yb-fiber laser with 3-GHz repetition-rate [19]. The mode-locking, initiated by a back-thinned saturable absorber mirror, lasts for a test period of >30 days. Long-term stability can be further improved by careful engineering. We are stabilizing the laser's repetition rate and the carrier-envelope offset frequency to achieve a frequency comb with 3-GHz line spacing.

Appendices

In the seven following appendices, we present analytic modeling for the seven filtering schemes listed in Table 1.

Appendix A:

scheme 1—*single FP filtering cavity followed by the CPA fiber amplifier*. The FP cavity has an FSR $f_{FSR} = Mf_{rs}$ where f_{rs} is the source-comb line spacing (i.e., the repetition rate of the source-comb laser).

Following the first two steps of the modeling procedure outlined in section 3.1, the filtered astro-comb after the FP filtering cavity is given by

$$\tilde{A}_a(\omega) = \tilde{A}_s(\omega)t_{FP} = \tilde{A}_0(\omega) \frac{1-R}{1-e^{-j\omega/f_{rs}}R} \sum_{l=-\infty}^{+\infty} \delta(\omega - l\omega_{rs}) = \tilde{A}_0(\omega) \frac{1-R}{1-e^{-j\omega T_{ra}}R} \sum_{l=-\infty}^{+\infty} \delta(\omega - l\omega_{rs}), \quad (\text{A1})$$

where $f_{ra} = f_{FSR}$ is the resulting astro-comb spectral line spacing and $T_{ra} = 1/f_{ra}$. By writing Eq. (A1), we assumed that the resulting astro-comb lines are aligned with the resonances of the FP filtering cavity, and experience full transmission; that is, at any astro-comb frequency $N\omega_{ra}$, we have $\tilde{A}_a(N\omega_{ra}) = \tilde{A}_0(N\omega_{ra})$.

To model the CPA fiber amplifier (i.e., steps (3) and (4) in section 3.1), we rewrite Eq. (A1) as

$$\tilde{A}_a(\omega) = \tilde{A}_0(\omega) \frac{1-R}{1-R^M} \frac{1-e^{-j\omega M T_{ra}} R^M}{1-e^{-j\omega T_{ra}} R} \sum_{l=-\infty}^{+\infty} \delta(\omega - l\omega_{rs}). \quad (\text{A2})$$

In writing Eq. (A2), we used the fact that $e^{-j\omega_s MT_m} = 1$ and nonzero spectral components exist only at the discrete angular frequencies: $0, \pm\omega_s, \pm 2\omega_s, \dots$. Using the equality

$$\frac{1 - e^{-j\omega MT_m} R^M}{1 - e^{-j\omega T_m} R} = \sum_{n=0}^{M-1} R^n e^{-jn\omega T_m},$$

Equation (A2) can be rewritten as

$$\begin{aligned} \tilde{A}_a(\omega) &= \frac{1-R}{1-R^M} \tilde{A}_0(\omega) \left(\sum_{n=0}^{M-1} R^n e^{-jn\omega T_m} \right) \sum_{l=-\infty}^{+\infty} \delta(\omega - l\omega_s) \\ &= \frac{1-R}{1-R^M} \tilde{A}_0(\omega) \left[\sum_{l=-\infty}^{+\infty} \delta(\omega - l\omega_s) + e^{-j\omega T_m} R \sum_{l=-\infty}^{+\infty} \delta(\omega - l\omega_s) + \dots + e^{-j\omega(M-1)T_m} R^{M-1} \sum_{l=-\infty}^{+\infty} \delta(\omega - l\omega_s) \right] \quad (\text{A3}) \\ &= \tilde{A}_0^s(\omega) \sum_{l=-\infty}^{+\infty} \delta(\omega - l\omega_s) + \tilde{A}_1^s(\omega) e^{-j\omega T_m} \sum_{l=-\infty}^{+\infty} \delta(\omega - l\omega_s) + \dots + \tilde{A}_{M-1}^s(\omega) e^{-j\omega(M-1)T_m} \sum_{l=-\infty}^{+\infty} \delta(\omega - l\omega_s) \end{aligned}$$

where $\tilde{A}_n^s(\omega) = R^n \frac{1-R}{1-R^M} \tilde{A}_0(\omega)$. The inverse Fourier transform of Eq. (A3) generates the corresponding temporal pulse train,

$$A_a^s(t) = A_0^s(t) * \sum_{k=-\infty}^{+\infty} \delta(t - kT_{rs}) + A_1^s(t) * \sum_{k=-\infty}^{+\infty} \delta(t - kT_{rs} - T_m) + \dots + A_{M-1}^s(t) * \sum_{k=-\infty}^{+\infty} \delta(t - kT_{rs} - (M-1)T_m)$$

where the pulse envelope $A_m^s(t) = R^m \frac{1-R}{1-R^M} A_0(t)$, $m = 0, 1, \dots, M-1$. $A_0(t)$ is the Fourier transform of $\tilde{A}_0(\omega)$, i.e., $A_0(t) = \int_{-\infty}^{\infty} \tilde{A}_0(\omega) e^{j\omega t} d\omega$. The operator $*$ denotes the convolution.

The modulation period $T_{rs} = 1/f_{rs} = MT_m$; see Fig. 3. For each pulse $A_m^s(t)$, we can find the corresponding spectrum at the output of the CPA fiber amplifier using Eq. (6) in section 3.1:

$$\tilde{A}_m^{1,amp}(\omega) = \exp\left(\frac{gL}{2}\right) \tilde{A}_m^s(\omega) \exp\left(j\frac{\phi_{str}}{2}\omega^2\right) \exp(jB_{1,m}s_{1,m}(\omega)), \quad (\text{A4})$$

where $B_{1,m} = \gamma L_{eff} \max\left[|A_m^{str}(t)|^2\right] = \gamma L_{eff} \max\left[|R^m A_0^{str}(t)|^2\right] = R^{2m} B_{1,0}$. $s_m(\omega)$ is the normalized spectrum, given by $s_{1,m}(\omega) = |\tilde{A}_m^s(\omega)|^2 / \max|\tilde{A}_m^s(\omega)|^2 = s_0(\omega) = |\tilde{A}_0(\omega)|^2 / \max|\tilde{A}_0(\omega)|^2$. Therefore Eq. (A4) can be rewritten as

$$\tilde{A}_m^{1,amp}(\omega) = \exp\left(\frac{gL}{2}\right) \left(\frac{1-R}{1-R^M}\right) \tilde{A}_0(\omega) R^m \exp\left(j\frac{\phi_{str}}{2}\omega^2\right) \exp(jR^{2m} B_{1,0} s_0(\omega)). \quad (\text{A5})$$

Plugging Eq. (A5) into Eq. (6) (see step 5 in section 3.1) results in the spectrum of the amplified astro-comb,

$$\tilde{A}^{1,final}(\omega) = \left\{ \sum_{m=0}^{M-1} R^m \exp[-j\omega m T_m + jR^{2m} B_{1,0} s_0(\omega)] \right\} \left(\frac{1-R}{1-R^M}\right) \tilde{A}_0(\omega) \exp\left(\frac{gL + j\phi_{str}\omega^2}{2}\right) \sum_{l=-\infty}^{+\infty} \delta(\omega - l\omega_s). \quad (\text{A6})$$

Since the side mode suppression and the calibration error (see Eq. (2)) are determined by the power (not the phase) of comb-lines after amplification, and remain unchanged if the entire spectrum is multiplied by a constant, we can neglect the constant coefficients and the quadratic phase in Eq. (A6) to obtain a simplified expression:

$$\tilde{A}^1(\omega) = \left\{ \sum_{m=0}^{M-1} R^m \exp[-j\omega m T_m + jR^{2m} B_{1,0} s_0(\omega)] \right\} \tilde{A}_0(\omega) \sum_{l=-\infty}^{+\infty} \delta(\omega - l\omega_s). \quad (\text{A7})$$

Appendix B:

scheme 2—two identical FP filtering cavities with the CPA fiber amplifier between the two cavities. Both FP cavities have a FSR satisfying $f_{\text{FSR}} = Mf_s$ where f_s is the source-comb's line spacing (i.e., the repetition rate of the source-comb laser).

Adding an additional FP filtering cavity to scheme 1 leads to scheme 2. The final astro-comb spectrum of scheme 2 can, therefore, be easily obtained from Eq. (A7):

$$\tilde{A}^2(\omega) = \tilde{A}^1(\omega) \times t_{\text{FP}} = \frac{1-R}{1-e^{-j\omega T_m} R} \left\{ \sum_{m=0}^{M-1} R^m \exp[-j\omega m T_m + jR^{2m} B_{1,0} s_0(\omega)] \right\} \tilde{A}_0(\omega) \sum_{l=-\infty}^{+\infty} \delta(\omega - l\omega_s). \quad (\text{B1})$$

Appendix C:

scheme 3—two identical FP filtering cavities followed by the CPA fiber amplifier. Both FP cavities have a FSR satisfying $f_{\text{FSR}} = Mf_s$ and f_s is the source-comb's line spacing.

The filtered astro-comb after two identical FP filtering cavities can be written as

$$\tilde{A}_a^I(\omega) = \tilde{A}_s(\omega) t_{\text{FP}} t_{\text{FP}} = \tilde{A}_0(\omega) \frac{(1-R)^2}{(1-e^{-j\omega T_m} R)^2} \sum_{l=-\infty}^{+\infty} \delta(\omega - l\omega_s). \quad (\text{C1})$$

Using the equality $\frac{1-R^M}{1-e^{-j\omega T_m} R} = \frac{1-e^{-j\omega M T_m} R^M}{1-e^{-j\omega T_m} R} = \sum_{n=0}^{M-1} R^n e^{-jn\omega T_m}$, Eq. (C1) can be rewritten as

$$\tilde{A}_a^I(\omega) = \tilde{A}_0(\omega) \left(\frac{1-R}{1-R^M} \right)^2 \left(\frac{1-e^{-j\omega M T_m} R^M}{1-e^{-j\omega T_m} R} \right)^2 \sum_{l=-\infty}^{+\infty} \delta(\omega - l\omega_s) = \tilde{A}_0(\omega) \left(\frac{1-R}{1-R^M} \right)^2 \left(\sum_{n=0}^{M-1} R^n e^{-jn\omega T_m} \right)^2 \sum_{l=-\infty}^{+\infty} \delta(\omega - l\omega_s).$$

The key is to calculate $\left(\sum_{n=0}^{M-1} R^n e^{-jn\omega T_m} \right)^2 \sum_{l=-\infty}^{+\infty} \delta(\omega - l\omega_s)$:

$$\begin{aligned} & \left(\sum_{n=0}^{M-1} R^n e^{-jn\omega T_m} \right)^2 \sum_{l=-\infty}^{+\infty} \delta(\omega - l\omega_s) \\ &= \left(\sum_{n=0}^{M-1} R^n e^{-j2\pi \frac{n}{M} \frac{\omega}{\omega_s}} \right) \left(\sum_{n=0}^{M-1} R^n e^{-j2\pi \frac{n}{M} \frac{\omega}{\omega_s}} \right) \sum_{l=-\infty}^{+\infty} \delta(\omega - l\omega_s) \\ &= \left(\sum_{m=0}^{M-1} \sum_{k=0}^{M-1} R^{m+k} e^{-j2\pi \frac{m+k}{M} \frac{\omega}{\omega_s}} \right) \sum_{l=-\infty}^{+\infty} \delta(\omega - l\omega_s) \\ &= \left(\sum_{n=0}^{M-1} (n+1) R^n e^{-j2\pi \frac{n}{M} \frac{\omega}{\omega_s}} + \sum_{n=0}^{M-1} (M-n-1) R^{M+n} e^{-j2\pi \frac{M+n}{M} \frac{\omega}{\omega_s}} \right) \sum_{l=-\infty}^{+\infty} \delta(\omega - l\omega_s) \\ &= \left(\sum_{n=0}^{M-1} (n+1) R^n e^{-j2\pi \frac{n}{M} \frac{\omega}{\omega_s}} + \sum_{n=0}^{M-1} (M-n-1) R^{M+n} e^{-j2\pi \frac{n}{M} \frac{\omega}{\omega_s}} \right) \sum_{l=-\infty}^{+\infty} \delta(\omega - l\omega_s) \\ &= \left(\sum_{n=0}^{M-1} [(n+1) + (M-n-1) R^M] R^n e^{-j2\pi \frac{n}{M} \frac{\omega}{\omega_s}} \right) \sum_{l=-\infty}^{+\infty} \delta(\omega - l\omega_s). \end{aligned}$$

Therefore we have

$$\begin{aligned}
\tilde{A}_a^I(\omega) &= \left(\frac{1-R}{1-R^M} \right)^2 \tilde{A}_0(\omega) \left(\sum_{n=0}^{M-1} [(n+1) + (M-n-1)R^M] R^n e^{-j2\pi \frac{n}{M} \omega T_m} \right) \sum_{l=-\infty}^{+\infty} \delta(\omega - l\omega_s) \\
&= \left(\frac{1-R}{1-R^M} \right)^2 \tilde{A}_0(\omega) \left(\sum_{n=0}^{M-1} [(n+1) + (M-n-1)R^M] R^n e^{-jn\omega T_m} \right) \sum_{l=-\infty}^{+\infty} \delta(\omega - l\omega_s) \\
&= \left(\frac{1-R}{1-R^M} \right)^2 \tilde{A}_0(\omega) \left[\begin{aligned} &[1 + (M-1)R^M] \sum_{l=-\infty}^{+\infty} \delta(\omega - l\omega_s) + e^{-j\omega T_m} [2 + (M-2)R^M] R \sum_{l=-\infty}^{+\infty} \delta(\omega - l\omega_s) + \\ &\dots + e^{-j\omega(M-1)T_m} MR^{M-1} \sum_{l=-\infty}^{+\infty} \delta(\omega - l\omega_s) \end{aligned} \right] \\
&= \tilde{A}_0^I(\omega) \sum_{l=-\infty}^{+\infty} \delta(\omega - l\omega_s) + \tilde{A}_1^I(\omega) e^{-j\omega T_m} \sum_{l=-\infty}^{+\infty} \delta(\omega - l\omega_s) + \dots + \tilde{A}_{M-1}^I(\omega) e^{-j\omega(M-1)T_m} \sum_{l=-\infty}^{+\infty} \delta(\omega - l\omega_s),
\end{aligned}$$

where $\tilde{A}_m^I(\omega) = \rho_m R^m \left(\frac{1-R}{1-R^M} \right)^2 \tilde{A}_0(\omega)$, and $\rho_m = m+1 + (M-m-1)R^M$. Hence the corresponding temporal pulse train is

$$A_a^I(t) = \left(\frac{1-R}{1-R^M} \right)^2 \left[A_0^I(t) * \sum_{k=-\infty}^{+\infty} \delta(t - kT_m) + A_1^I(t) * \sum_{k=-\infty}^{+\infty} \delta(t - kT_m - T_m) + \dots + A_{M-1}^I(t) * \sum_{k=-\infty}^{+\infty} \delta(t - kT_m - (M-1)T_m) \right] \quad (C2)$$

where $A_m^I(t) = \rho_m R^m \left(\frac{1-R}{1-R^M} \right)^2 A_0(t)$. $A_0(t)$ is connected to $\tilde{A}_0(\omega)$ by Fourier transform,

i.e., $A_0(t) = \int_{-\infty}^{\infty} \tilde{A}_0(\omega) e^{j\omega t} d\omega$. For each individual pulse $A_m^I(t)$, we can find the corresponding spectrum at the output of the CPA fiber amplifier using Eq. (5) in section 3.1, leading to

$$\tilde{A}_m^{3,amp}(\omega) = \exp\left(\frac{gL}{2}\right) \tilde{A}_m^I(\omega) \exp\left(j\frac{\phi_{str}}{2}\omega^2\right) \exp(jB_{3,m}s_{3,m}(\omega)), \quad (C3)$$

where $B_{3,m} = \rho_m^2 R^{2m} B_{3,0}$. $s_{3,m}(\omega)$ is the normalized spectrum, given by $s_{3,m}(\omega) = |\tilde{A}_m^I(\omega)|^2 / \max |\tilde{A}_m^I(\omega)|^2 = s_0(\omega) = |\tilde{A}_0(\omega)|^2 / \max |\tilde{A}_0(\omega)|^2$. Thus Eq. (C3) can be rewritten as

$$\tilde{A}_m^{3,amp}(\omega) = \exp\left(\frac{gL}{2}\right) \left(\frac{1-R}{1-R^M} \right)^2 \tilde{A}_0(\omega) \rho_m R^m \exp\left(j\frac{\phi_{str}}{2}\omega^2\right) \exp(j\rho_m^2 R^{2m} B_{3,0} s_0(\omega)). \quad (C4)$$

Plugging Eq. (B4) into Eq. (6) results in the spectrum of the amplified astro-comb,

$$\tilde{A}^{3,final}(\omega) = \left\{ \sum_{m=0}^{M-1} \rho_m R^m \exp[-j\omega m T_m + j\rho_m^2 R^{2m} B_{3,0} s_0(\omega)] \right\} \left(\frac{1-R}{1-R^M} \right)^2 \tilde{A}_0(\omega) \exp\left(\frac{gL + j\phi_{str}\omega^2}{2}\right) \sum_{l=-\infty}^{+\infty} \delta(\omega - l\omega_s). \quad (C5)$$

Neglecting the constant coefficients and the quadratic phase in Eq. (C5) leads to the simplified expression:

$$\tilde{A}^3(\omega) = \left\{ \sum_{m=0}^{M-1} \rho_m R^m \exp[-j\omega m T_m + j\rho_m^2 R^{2m} B_{3,0} s_0(\omega)] \right\} \tilde{A}_0(\omega) \sum_{l=-\infty}^{+\infty} \delta(\omega - l\omega_s). \quad (C6)$$

Appendix D:

scheme 4—two co-prime FP filtering cavities with the CPA fiber amplifier in between. These FP cavities have their FSR satisfying $f_{FSR1} = M_1 f_{rs}$ and $f_{FSR2} = M_2 f_{rs}$, respectively. M_1 and M_2 are co-prime with each other; f_{rs} is the source-comb's line spacing.

For two FP filtering cavities with their FSR set as $f_{FSR1} = M_1 f_{rs}$ and $f_{FSR2} = M_2 f_{rs}$, the transmission of these cascade cavities results in an increase of comb spacing by a factor of $M = M_1 M_2$ if M_1 and M_2 are co-prime with each other. From Appendix A, we know that the amplified astro-comb after the CPA amplifier is given by

$$\tilde{A}^{4,amp}(\omega) = \left\{ \sum_{m=0}^{M_1-1} R^m \exp[-j\omega m T_{ra} + jR^{2m} B_{4,0} s_0(\omega)] \right\} \left(\frac{1-R}{1-R^{M_1}} \right) \tilde{A}_0(\omega) \exp\left(\frac{gL + j\phi_{gr} \omega^2}{2}\right) \sum_{l=-\infty}^{+\infty} \delta(\omega - l \omega_{rs}).$$

Then the final astro-comb after the 2nd FP filtering cavity is given by

$$\tilde{A}^{4,final}(\omega) = \tilde{A}^{4,amp}(\omega) \times t_{FP2} = \frac{1-R}{1-e^{-j\omega T_{ra2}} R} \tilde{A}^{4,amp}(\omega), \text{ with } T_{ra2} = T_{rs} / M_2 = 1 / (f_{rs} M_2).$$

That is,

$$\tilde{A}^{4,amp}(\omega) = \frac{1-R}{1-e^{-j\omega T_{ra}/M_2} R} \left\{ \sum_{m=0}^{M_1-1} R^m \exp[-j\omega m T_{ra} + jR^{2m} B_{4,0} s_0(\omega)] \right\} \left(\frac{1-R}{1-R^{M_1}} \right) \tilde{A}_0(\omega) \exp\left(\frac{gL + j\phi_{gr} \omega^2}{2}\right) \sum_{l=-\infty}^{+\infty} \delta(\omega - l \omega_{rs}). \quad (D1)$$

Neglecting the constant coefficients and the quadratic phase in Eq. (D1) leads to the simplified expression:

$$\tilde{A}^4(\omega) = \frac{1-R}{1-e^{-j\omega T_{ra}/M_2} R} \left\{ \sum_{m=0}^{M_1-1} R^m \exp[-j\omega m T_{ra} + jR^{2m} B_{4,0} s_0(\omega)] \right\} \tilde{A}_0(\omega) \sum_{l=-\infty}^{+\infty} \delta(\omega - l \omega_{rs}). \quad (D2)$$

Appendix E:

scheme 5—two co-prime FP filtering cavities followed by the CPA fiber amplifier. These FP cavities have their FSR satisfying $f_{FSR1} = M_1 f_{rs}$ and $f_{FSR2} = M_2 f_{rs}$, respectively. M_1 and M_2 are co-prime with each other; f_{rs} is the source-comb's line spacing.

The filtered astro-comb after two co-prime FP filtering cavities can be written as

$$\tilde{A}_a^C(\omega) = \tilde{A}_s(\omega) t_{FP1} t_{FP2} = \tilde{A}_0(\omega) \frac{1-R}{(1-e^{-j\omega T_{ra1}} R)} \frac{1-R}{(1-e^{-j\omega T_{ra2}} R)} \sum_{l=-\infty}^{+\infty} \delta(\omega - l \omega_{rs}), \quad (E1)$$

where $T_{rs} = M_1 T_{ra1} = M_2 T_{ra2}$. M_1 and M_2 are co-prime, and $M = M_1 M_2$. Using the equality

$$\frac{1-R^M}{1-e^{-j\omega T_{ra1}} R} = \frac{1-e^{-j\omega M T_{ra1}} R^M}{1-e^{-j\omega T_{ra1}} R} = \sum_{n=0}^{M-1} R^n e^{-jn\omega T_{ra1}} \quad \text{and} \quad \frac{1-R^M}{1-e^{-j\omega T_{ra2}} R} = \frac{1-e^{-j\omega M T_{ra2}} R^M}{1-e^{-j\omega T_{ra2}} R} = \sum_{k=0}^{M-1} R^k e^{-jk\omega T_{ra2}}, \quad \text{Eq.}$$

(E1) can be rewritten as

$$\begin{aligned} \tilde{A}_a^C(\omega) &= \tilde{A}_0(\omega) \frac{(1-R)^2}{(1-R^M)^2} \frac{1-e^{-j\omega M T_{ra1}} R^M}{(1-e^{-j\omega T_{ra1}} R)} \frac{1-e^{-j\omega M T_{ra2}} R^M}{(1-e^{-j\omega T_{ra2}} R)} \sum_{l=-\infty}^{+\infty} \delta(\omega - l \omega_{rs}) \\ &= \tilde{A}_0(\omega) \left(\frac{1-R}{1-R^M} \right)^2 \left(\sum_{n=0}^{M-1} R^n e^{-jn\omega T_{ra1}} \right) \left(\sum_{k=0}^{M-1} R^k e^{-jk\omega T_{ra2}} \right) \sum_{l=-\infty}^{+\infty} \delta(\omega - l \omega_{rs}) \\ &= \tilde{A}_0(\omega) \left(\frac{1-R}{1-R^M} \right)^2 \left(\sum_{n=0}^{M-1} R^n e^{-j2\pi \frac{n}{M_1} \frac{\omega}{\omega_{rs}}} \right) \left(\sum_{k=0}^{M-1} R^k e^{-j2\pi \frac{k}{M_2} \frac{\omega}{\omega_{rs}}} \right) \sum_{l=-\infty}^{+\infty} \delta(\omega - l \omega_{rs}) \end{aligned}$$

Note that

$$\begin{aligned}
& \left(\sum_{n=0}^{M-1} R^n e^{-j 2\pi \frac{n}{M_1} \frac{\omega}{\omega_s}} \right) \sum_{l=-\infty}^{+\infty} \delta(\omega - l \omega_s) \\
&= \left(\sum_{n=0}^{M_1-1} R^n e^{-j 2\pi \frac{n}{M_1} \frac{\omega}{\omega_s}} + \sum_{n=0}^{M_1-1} R^{n+M_1} e^{-j 2\pi \frac{n}{M_1} \frac{\omega}{\omega_s}} + \sum_{n=0}^{M_1-1} R^{n+2M_1} e^{-j 2\pi \frac{n}{M_1} \frac{\omega}{\omega_s}} + \dots + \sum_{n=0}^{M_1-1} R^{n+(M_2-1)M_1} e^{-j 2\pi \frac{n}{M_1} \frac{\omega}{\omega_s}} \right) \sum_{l=-\infty}^{+\infty} \delta(\omega - l \omega_s) \\
&= \left(\sum_{n=0}^{M_1-1} [R^n + R^{n+M_1} + R^{n+2M_1} + \dots + R^{n+(M_2-1)M_1}] e^{-j 2\pi \frac{n}{M_1} \frac{\omega}{\omega_s}} \right) \sum_{l=-\infty}^{+\infty} \delta(\omega - l \omega_s) \\
&= \left(\sum_{n=0}^{M_1-1} \frac{1-R^{M_2 M_1}}{1-R^{M_1}} R^n e^{-j 2\pi \frac{n}{M_1} \frac{\omega}{\omega_s}} \right) \sum_{l=-\infty}^{+\infty} \delta(\omega - l \omega_s) \\
&= \left(\sum_{n=0}^{M_1-1} R^n e^{-j 2\pi \frac{n}{M_1} \frac{\omega}{\omega_s}} \right) \frac{1-R^M}{1-R^{M_1}} \sum_{l=-\infty}^{+\infty} \delta(\omega - l \omega_s)
\end{aligned}$$

Therefore we have

$$\begin{aligned}
& \left(\sum_{n=0}^{M-1} R^n e^{-j 2\pi \frac{n}{M_1} \frac{\omega}{\omega_s}} \right) \left(\sum_{k=0}^{M-1} R^k e^{-j 2\pi \frac{k}{M_2} \frac{\omega}{\omega_s}} \right) \sum_{l=-\infty}^{+\infty} \delta(\omega - l \omega_s) \\
&= \left(\sum_{n=0}^{M_1-1} R^n e^{-j 2\pi \frac{n}{M_1} \frac{\omega}{\omega_s}} \right) \left(\sum_{k=0}^{M_2-1} R^k e^{-j 2\pi \frac{k}{M_2} \frac{\omega}{\omega_s}} \right) \frac{1-R^M}{1-R^{M_1}} \frac{1-R^M}{1-R^{M_2}} \sum_{l=-\infty}^{+\infty} \delta(\omega - l \omega_s) \\
&= \left(\sum_{n=0}^{M_1-1} \sum_{k=0}^{M_2-1} R^{n+k} e^{-j 2\pi \left(\frac{n}{M_1} + \frac{k}{M_2} \right) \frac{\omega}{\omega_s}} \right) \frac{(1-R^M)^2}{(1-R^{M_1})(1-R^{M_2})} \sum_{l=-\infty}^{+\infty} \delta(\omega - l \omega_s) \\
&= \left(\sum_{m=0}^{M-1} R^{p(m)} e^{-j 2\pi \frac{m}{M} \frac{\omega}{\omega_s}} \right) \frac{(1-R^M)^2}{(1-R^{M_1})(1-R^{M_2})} \sum_{l=-\infty}^{+\infty} \delta(\omega - l \omega_s)
\end{aligned}$$

where $p(m) = n + k$ with n and k subject to $\text{mod}(M_2 n + M_1 k, M) = m$. Therefore we have

$$\tilde{A}_a^C(\omega) = \tilde{A}_s(\omega) t_{FP1} t_{FP2} = \left(\sum_{m=0}^{M-1} R^{p(m)} e^{-j 2\pi \frac{m}{M} \frac{\omega}{\omega_s}} \right) \frac{(1-R^M)^2}{(1-R^{M_1})(1-R^{M_2})} \tilde{A}_0(\omega) \sum_{l=-\infty}^{+\infty} \delta(\omega - l \omega_s) \quad (\text{E2})$$

Using the fact that $T_{ra} = 2\pi / (M \omega_s)$, we can further write Eq. (B2) as

$$\tilde{A}_a^C(\omega) = \frac{(1-R)^2}{(1-R^{M_1})(1-R^{M_2})} \tilde{A}_0(\omega) \left[R^{p(0)} \sum_{l=-\infty}^{+\infty} \delta(\omega - l\omega_{rs}) + e^{-j\omega T_{ra}} R^{p(1)} \sum_{l=-\infty}^{+\infty} \delta(\omega - l\omega_{rs}) + \dots \right. \\ \left. + e^{-j\omega(M-1)T_{ra}} R^{p(M-1)} \sum_{l=-\infty}^{+\infty} \delta(\omega - l\omega_{rs}) \right]$$

$$= \tilde{A}_0^C(\omega) \sum_{l=-\infty}^{+\infty} \delta(\omega - l\omega_{rs}) + \tilde{A}_1^C(\omega) e^{-j\omega T_{ra}} \sum_{l=-\infty}^{+\infty} \delta(\omega - l\omega_{rs}) + \dots + \tilde{A}_{M-1}^C(\omega) e^{-j\omega(M-1)T_{ra}} \sum_{l=-\infty}^{+\infty} \delta(\omega - l\omega_{rs})$$

where $\tilde{A}_m^C(\omega) = R^{p(m)} \frac{(1-R)^2}{(1-R^{M_1})(1-R^{M_2})} \tilde{A}_0(\omega)$ and $m = 0, 1, \dots, M-1$.

Hence the corresponding temporal pulse train is

$$A_a^C(t) = A_0^C(t) * \sum_{k=-\infty}^{+\infty} \delta(t - kT_{ra}) + A_1^C(t) * \sum_{k=-\infty}^{+\infty} \delta(t - kT_{ra} - T_{ra}) + \dots + A_{M-1}^C(t) * \sum_{k=-\infty}^{+\infty} \delta(t - kT_{ra} - (M-1)T_{ra}) \quad (\text{E3})$$

where pulse envelope $A_m^C(t) = R^{p(m)} \frac{(1-R)^2}{(1-R^{M_1})(1-R^{M_2})} A_0(t)$, and $m = 0, 1, \dots, M-1$.

Taking Eq. (E3) as the input to the CPA amplifier and following a similar derivation from Eq. (C3) to (C6) in Appendix C, we can find the spectrum of the amplified astro-comb, which is given by

$$\tilde{A}^{s,final}(\omega) = \left\{ \sum_{m=0}^{M-1} R^{p(m)} \exp[-j\omega m T_{ra} + jR^{2p(m)} B_{5,0} s_0(\omega)] \right\} \frac{(1-R)^2 \tilde{A}_0(\omega)}{(1-R^{M_1})(1-R^{M_2})} \exp\left(\frac{gL + j\phi_{gr}\omega^2}{2}\right) \sum_{l=-\infty}^{+\infty} \delta(\omega - l\omega_{rs}).$$

Neglecting the constant coefficients and the quadratic phase in the above equation leads to the simplified expression:

$$\tilde{A}^5(\omega) = \left\{ \sum_{m=0}^{M-1} R^{p(m)} \exp[-j\omega m T_{ra} + jR^{2p(m)} B_{5,0} s_0(\omega)] \right\} \tilde{A}_0(\omega) \sum_{l=-\infty}^{+\infty} \delta(\omega - l\omega_{rs}). \quad (\text{E4})$$

Appendix F:

scheme 6—two fraction-prime FP filtering cavities with the CPA fiber amplifier in between. These FP cavities have their FSR satisfying $f_{FSR1} = Mf_{rs}$ and $f_{FSR2} = (M/N)f_{rs}$, respectively. M and N are co-prime.

Following the derivation in Appendix D, we can find the astro-comb after the 2nd FP filtering cavity, given by

$$\tilde{A}^6(\omega) = \frac{1-R}{1-e^{-j\omega T_{ra} N/M} R} \left\{ \sum_{m=0}^{M-1} R^m \exp[-j\omega m T_{ra} + jR^{2m} B_{6,0} s_0(\omega)] \right\} \tilde{A}_0^s(\omega) \sum_{l=-\infty}^{+\infty} \delta(\omega - l\omega_{rs}). \quad (\text{F1})$$

Appendix G:

scheme 7—two fraction-prime FP filtering cavities followed by the CPA fiber amplifier. These FP cavities have their FSR satisfying $f_{FSR1} = Mf_{rs}$ and $f_{FSR2} = (M/N)f_{rs}$, respectively. M and N are co-prime.

After the two fraction-prime FP filtering cavities, the filtered astro-comb can be written as

$$\tilde{A}_a^F(\omega) = \tilde{A}_s(\omega) t_{FP1} t_{FP2} = \tilde{A}_0(\omega) \frac{1-R}{(1-e^{-j\omega T_{ra} M} R)} \frac{1-R}{(1-e^{-j\omega T_{ra} N} R)} \sum_{l=-\infty}^{+\infty} \delta(\omega - l\omega_{rs}) \quad (\text{G1})$$

where $T_{rs} = MT_{m1} = (M/N)T_{m2}$. M and N are co-prime. Using the equality $\frac{1-R^M}{1-e^{-j\omega T_{m1}}R} = \frac{1-e^{-j\omega MT_{m1}}R^M}{1-e^{-j\omega T_{m1}}R} = \sum_{n=0}^{M-1} R^n e^{-jn\omega T_{m1}}$ and $\frac{1-R^M}{1-e^{-j\omega T_{m2}}R} = \frac{1-e^{-j\omega MT_{m2}}R^M}{1-e^{-j\omega T_{m2}}R} = \sum_{k=0}^{M-1} R^k e^{-jk\omega T_{m2}}$, Eq. (G1) can be rewritten as

$$\begin{aligned}\tilde{A}_a^F(\omega) &= \tilde{A}_0(\omega) \frac{(1-R)^2}{(1-R^M)^2} \frac{1-e^{-j\omega MT_{m1}}R^M}{(1-e^{-j\omega T_{m1}}R)} \frac{1-e^{-j\omega MT_{m2}}R^M}{(1-e^{-j\omega T_{m2}}R)} \sum_{l=-\infty}^{+\infty} \delta(\omega-l\omega_{rs}) \\ &= \tilde{A}_0(\omega) \left(\frac{1-R}{1-R^M} \right)^2 \left(\sum_{n=0}^{M-1} R^n e^{-jn\omega T_{m1}} \right) \left(\sum_{k=0}^{M-1} R^k e^{-jk\omega T_{m2}} \right) \sum_{l=-\infty}^{+\infty} \delta(\omega-l\omega_{rs}) \quad (\text{G2}) \\ &= \tilde{A}_0(\omega) \left(\frac{1-R}{1-R^M} \right)^2 \left(\sum_{n=0}^{M-1} R^n e^{-j2\pi \frac{n}{M} \frac{\omega}{\omega_{rs}}} \right) \left(\sum_{k=0}^{M-1} R^k e^{-j2\pi \frac{Nk}{M} \frac{\omega}{\omega_{rs}}} \right) \sum_{l=-\infty}^{+\infty} \delta(\omega-l\omega_{rs}).\end{aligned}$$

Let $m = \text{mod}(Nk, M)$. Since M and N are co-prime, there exists such $0 \leq k_0 \leq M-1$ that $\text{mod}(Nk_0, M) = 1$. Therefore, k and m can be connected by $k = f(m) = \text{mod}(mk_0, M)$.

Therefore we have

$$\left(\sum_{k=0}^{M-1} R^k e^{-j2\pi \frac{Nk}{M} \frac{\omega}{\omega_{rs}}} \right) \sum_{l=-\infty}^{+\infty} \delta(\omega-l\omega_{rs}) = \left(\sum_{m=0}^{M-1} R^{f(m)} e^{-j2\pi \frac{m}{M} \frac{\omega}{\omega_{rs}}} \right) \sum_{l=-\infty}^{+\infty} \delta(\omega-l\omega_{rs}).$$

Eq. (G2) can be further calculated as

$$\begin{aligned}\tilde{A}_0(\omega) &\left(\frac{1-R}{1-R^M} \right)^2 \left(\sum_{n=0}^{M-1} R^n e^{-j2\pi \frac{n}{M} \frac{\omega}{\omega_{rs}}} \right) \left(\sum_{m=0}^{M-1} R^{f(m)} e^{-j2\pi \frac{m}{M} \frac{\omega}{\omega_{rs}}} \right) \sum_{l=-\infty}^{+\infty} \delta(\omega-l\omega_{rs}) \\ &= \tilde{A}_0(\omega) \left(\frac{1-R}{1-R^M} \right)^2 \left(\sum_{n=0}^{M-1} \sum_{m=0}^{M-1} R^{n+f(m)} e^{-j2\pi \frac{n+m}{M} \frac{\omega}{\omega_{rs}}} \right) \sum_{l=-\infty}^{+\infty} \delta(\omega-l\omega_{rs}) \quad (\text{G3}) \\ &= \tilde{A}_0(\omega) \left(\frac{1-R}{1-R^M} \right)^2 \left(\sum_{n=0}^{M-1} \left[\sum_{i=0}^n R^{i+f(n-i)} e^{-j2\pi \frac{n}{M} \frac{\omega}{\omega_{rs}}} \right] + \sum_{n=0}^{M-1} \left[\sum_{i=n+1}^{M-1} R^{i+f(M+n-i)} e^{-j2\pi \frac{M+n}{M} \frac{\omega}{\omega_{rs}}} \right] \right) \sum_{l=-\infty}^{+\infty} \delta(\omega-l\omega_{rs}) \\ &= \tilde{A}_0(\omega) \left(\frac{1-R}{1-R^M} \right)^2 \left(\sum_{n=0}^{M-1} \left[\sum_{i=0}^n R^{i+f(n-i)} + \sum_{i=n+1}^{M-1} R^{i+f(M+n-i)} \right] e^{-j2\pi \frac{n}{M} \frac{\omega}{\omega_{rs}}} \right) \sum_{l=-\infty}^{+\infty} \delta(\omega-l\omega_{rs}) \\ &= \tilde{A}_0(\omega) \left(\frac{1-R}{1-R^M} \right)^2 \left(\sum_{n=0}^{M-1} \eta(n) e^{-j2\pi \frac{n}{M} \frac{\omega}{\omega_{rs}}} \right) \sum_{l=-\infty}^{+\infty} \delta(\omega-l\omega_{rs}),\end{aligned}$$

where $\eta(n) = \sum_{i=0}^n R^{i+f(n-i)} + \sum_{i=n+1}^{M-1} R^{i+f(M+n-i)}$.

Using the fact that $T_{m1} = 2\pi / (M\omega_{rs})$, we can further write Eq. (G3) as

$$\begin{aligned}\tilde{A}_a^F(\omega) &= \left(\frac{1-R}{1-R^M} \right)^2 \tilde{A}_0(\omega) \left[\begin{aligned} &\eta(0) \sum_{l=-\infty}^{+\infty} \delta(\omega-l\omega_{rs}) + e^{-j\omega T_{m1}} \eta(1) \sum_{l=-\infty}^{+\infty} \delta(\omega-l\omega_{rs}) + \dots \\ &+ e^{-j\omega(M-1)T_{m1}} \eta(M-1) \sum_{l=-\infty}^{+\infty} \delta(\omega-l\omega_{rs}) \end{aligned} \right] \\ &= \tilde{A}_0^F(\omega) \sum_{l=-\infty}^{+\infty} \delta(\omega-l\omega_{rs}) + \tilde{A}_1^F(\omega) e^{-j\omega T_{m1}} \sum_{l=-\infty}^{+\infty} \delta(\omega-l\omega_{rs}) + \dots + \tilde{A}_{M-1}^F(\omega) e^{-j\omega(M-1)T_{m1}} \sum_{l=-\infty}^{+\infty} \delta(\omega-l\omega_{rs}) \\ &\text{where } \tilde{A}_m^F(\omega) = \eta(m) \left(\frac{1-R}{1-R^M} \right)^2 \tilde{A}_0(\omega), \text{ and } m = 0, 1, \dots, M-1.\end{aligned}$$

Hence the corresponding temporal pulse train is

$$A_a^F(t) = A_0^F(t) * \sum_{k=-\infty}^{+\infty} \delta(t - kT_{rs}) + A_1^F(t) * \sum_{k=-\infty}^{+\infty} \delta(t - kT_{rs} - T_m) + \dots + A_{M-1}^F(t) * \sum_{k=-\infty}^{+\infty} \delta(t - kT_{rs} - (M-1)T_m) \quad (\text{G4})$$

where pulse envelope $A_m^F(t) = \eta(m) \left(\frac{1-R}{1-R^M} \right)^2 A_0(t)$, and $m = 0, 1, \dots, M-1$. Taking Eq. (G4)

as the input to the CPA amplifier and following a similar derivation from Eq. (C3) to (C6) in Appendix C, we can find the spectrum of the amplified astro-comb, given by

$$\tilde{A}^{\text{final}}(\omega) = \left\{ \sum_{m=0}^{M-1} \eta(m) \exp[-j\omega m T_m + j\eta(m) B_{7,0} s_0(\omega)] \right\} \left(\frac{1-R}{1-R^M} \right)^2 \tilde{A}_0(\omega) \exp\left(\frac{gL + j\phi_{str} \omega^2}{2}\right) \sum_{l=-\infty}^{+\infty} \delta(\omega - l\omega_{rs}).$$

Neglecting the constant coefficients and the quadratic phase in the above equation leads to the simplified expression:

$$\tilde{A}^7(\omega) = \left\{ \sum_{m=0}^{M-1} \eta(m) \exp[-j\omega m T_m + j\eta(m) B_{7,0} s_0(\omega)] \right\} \tilde{A}_0(\omega) \sum_{l=-\infty}^{+\infty} \delta(\omega - l\omega_{rs}). \quad (\text{G5})$$

Acknowledgments

This work was supported by the National Aeronautics and Space Administration (NASA) through grants NNX10AE68G, NNX09AC92G and by the National Science Foundation (NSF) through grants AST-0905592 and AST-1006507 and the Center for Free-Electron Laser Science. The authors thank Damian N. Schimpf for helpful discussion.